UC San Diego

UC San Diego Electronic Theses and Dissertations

Title

Numerical Methods for Continuum Mechanics with Nonlocal Interactions: Weak Form Peridynamics and Nanoscale Strain Engineering

Permalink

https://escholarship.org/uc/item/4zp401vn

Author

Shen, Zhaoxiang

Publication Date

2021

Peer reviewed|Thesis/dissertation

eScholarship.org Powered by the California Digital Library
University of California

UNIVERSITY OF CALIFORNIA SAN DIEGO

Numerical Methods for Continuum Mechanics with Nonlocal Interactions: Weak Form Peridynamics and Nanoscale Strain Engineering

A thesis submitted in partial satisfaction of the
requirements for the degree
Master of Science

in

Engineering Science (Mechanical Engineering)

by

Zhaoxiang Shen

Committee in charge:

Professor David Kamensky, Chair
Professor Boris Kramer
Professor Ellad Tadmor
Professor Xiaochuan Tian

2021

Copyright
Zhaoxiang Shen, 2021
All rights reserved.

The thesis of Zhaoxiang Shen is approved, and it is acceptable in quality and form for publication on microfilm and electronically.

University of California San Diego

2021

DEDICATION

To my family.

TABLE OF CONTENTS

LIST OF FIGURES

LIST OF TABLES

ACKNOWLEDGEMENTS

First, I would like to thank my advisor, Professor David Kamensky for his support and guidance, for leading me to my first formal research experience, and for providing me an opportunity to be a TA. Thanks are also extended to Professor Boris Kramer, Professor Ellad Tadmor and Professor Xiaochuan Tian for serving on my committee and for sharing their knowledge with me. Thanks to Dr. Nathaniel Trask and Dr. Marta D'Elia for the great collaboration on the peridynamics project. Also thanks to Moon-ki Choi for the great collaboration on the strain engineering project. I would also like to express my sincere gratitude to my co-worker and friend, Dr. Marco Pasetto, for mentoring me during the research and helping me overcome lots of challenges, although we only met once in person due to the pandemic.

As an international student, this journey supposes to be more colorful and active. The pandemic is really an unexpected challenge for everyone. Thanks to my friends, Ruochen Ma, Yanzhang Deng, Jiheng Wang, Yulin Li, Mufeng Xie, Shuo Tan, Li Xing, You Jiang and Zhili Chen for their friendship and support during this difficult time.

At last, I would express my best thanks to my family for believing in me and for their unquestioning support and love.

ABSTRACT OF THE THESIS

Numerical Methods for Continuum Mechanics with Nonlocal Interactions: Weak Form Peridynamics and Nanoscale Strain Engineering

by

Zhaoxiang Shen

Master of Science in Engineering Science (Mechanical Engineering)

University of California San Diego, 2021

Professor David Kamensky, Chair

Nonlocal interactions raise numerical challenges such as high computational cost and geometric complexity. In the context of continuum mechanics, this thesis studies numerical methods for two nonlocal problems: weak form peridynamics and nanoscale strain engineering.

Unlike the classical local theory, the weak formulation of peridynamics involves a double integral and the additional integral operator needs an efficient quadrature rule. For this reason, the thesis investigates convergence behaviours of a promising quadrature rule

based on Generalized Moving Least Squares (GMLS) when applied to the double integral. For uniform discretizations, second-order convergence is observed with a mesh extension for global symmetrical inner quadrature. For non-uniform discretizations, a proposed strategy for symmetrically placing inner quadrature points shows decaying second-order convergence, while increasing the number of outer quadrature points leads to a more persistent convergence behaviour. Numerical tests in 1D demonstrate the above properties and 2D tests show consistent behaviours.

Nanoscale strain engineering aims at tuning the electronic properties of a semiconductor by modulating its nanoscale stain field, and the nonlocal interaction through Van der Waals forces is a possible mechanism for the modulation. To better understand the interaction process, based on the Lennard-Jones (LJ) model, the thesis builds a continuum model to simulate nonlocal interactions between a monolayer MoS_2 and a multihole Si_3N_4 substrate. A low-dimensional model is first built as a proof of concept before considering the real problem. The monolayer MoS_2 is then modeled by a Kirchhoff–Love shell while the integration of LJ potential over the substrate is approximated by a Riemann sum in a finite range and optimized using octrees. An alternative approach based on a semi-infinite integral is proposed for the integration over curved substrates, as a preliminary study for future work.

Chapter 1

Introduction

1.1 Motivation

The nonlocal interaction is the concept that an object can interact with another object but without physical touch. Gravity and magnetism are simple examples that show nonlocality. A problem that involves nonlocal interactions is referred to as a nonlocal problem. Nonlocality not only leads to an appropriate modeling for atomistic systems, but is also capable of relaxing the regularity requirements of differential models by the integral form while capturing long-range effects. This broadens the applicability of nonlocal models from microscale to macroscale such as fracture and contact.

Nonlocal problems raise many computational challenges. For nonlocal continuum models, challenges include the discretization of nonlocal systems, the construction of quadrature rules for integral operators and so on. Nonetheless, for atomistic models, the discrete nature brings additional computational costs that are always extremely expensive. This

thesis aims to investigate numerical methods that are efficient for nonlocal problems in the context of continuum mechanics, and focuses on two topics: **weak form peridynamics** and **nanoscale strain engineering**.

The peridynamic theory is an integro-differential nonlocal reformulation of classical theory of continuum solid mechanics (see Section 1.2). In conjunction with finite element approximations (see Section 2.1), the strong form perdynamics needs to be recast into the weak (variational) form which entails a double integral. Due to the presence of an additional integral operator, the application of weak form peridynamics is computationally expensive and involves high geometric complexity. A quadrature rule based on Generalized Moving least Squares (GMLS) (see Section 3.3) was proposed for general nonlocal models. Considering its high-order convergence and low computational cost, the GMLS-based method is a potentially efficient solution for the challenge raised by weak form peridynamics, which leads to the convergence study of GMLS-based method in this thesis.

The nanoscale strain engineering is a general strategy in the material world to enhance semiconductor performance. By modulating strain field of the material at nanoscale, the electronic properties can be tuned as desired. In conjunction with the strain engineering, a popular transition metal dichalcogenide, MoS_2, has attracted considerable attention for its outstanding properties with multilayer structure [1, 2, 3, 4]. While the nonlocal interaction governed by Van der Waals force is possible mechanism for strain engineering, it's important to understand the interaction process between MoS_2 and other common materials. The molecular dynamics (MD) is a traditional approach to simulate such atom-

istic problem and the Lennard-Jones model (see Section 1.3) is often used to approximate Van der Waals force. However, the discrete nature of MD limits simulation scale and exaggerates computational costs. Considering the structure and potential deflections of a monolayer MoS_2, a continuum shell is a possible alternative approximation for it with significantly lower expense. Nonetheless, to become an alternative choice, the continuum model needs to be able to effectively reproduce MD simulations. For this motivation, this thesis builds continuum models to simulate nonlocal interactions between a monolayer MoS_2 and a multihole Si_3N_4 substrate (a common material) with the help of several numerical methods.

1.2 The peridynamic theory

The peridynamic theory [5, 6, 7, 8] is an integro-differential nonlocal reformulation of the classical theory of continuum solid mechanics. It was proposed in [5, 6] to deal with the spontaneous formation of discontinuities, such as cracks. In contrast to the classical theory requiring the differentiability assumption on displacement fields, peridynamics uses integration to compute balance laws and can thus be applied to discontinuity problems. Applications of peridynamics therefore include crack nucleation [9], crack propagation [10, 11], and failure and damage in composite laminates [8, 12], concrete [13], and polycrystals [14], among others.

The peridynamic theory is nonlocal since interactions between material points in the theory exist over finite distances. Given a bounded body $\Omega \subset \mathbb{R}^d$, where d is the spatial

dimension ($d = 1, 2, 3$), a material point $\mathbf{x} \in \Omega$ interacts with all neighbor points $\mathbf{x}' \in \mathbb{R}^d$ within its neighborhood:

$$\mathscr{H}(\mathbf{x}, \delta) := \left\{ \mathbf{x}' \in \mathbb{R}^d : \|\boldsymbol{\xi}\| \leq \delta \right\}, \tag{1.1}$$

where $\boldsymbol{\xi} := \mathbf{x}' - \mathbf{x}$ is called the bond that represents the relative position of the material point $\mathbf{x}'$ and the material point $\mathbf{x}$ in the reference configuration. In this thesis, it is assumed that the horizon δ is independent of the material point.

By replacing the stress divergence in the classical continuum mechanics model, the peridynamic equation of motion for a material point $\mathbf{x} \in \Omega$ at time $t \geq 0$ is defined as

$$\rho(\mathbf{x}) \frac{\partial^2 \mathbf{u}}{\partial t^2}(\mathbf{x}, t) = \int_{\mathscr{H}(\mathbf{x}, \delta)} \hat{\mathbf{f}}(\mathbf{x}, \mathbf{x}', t) d\mathbf{x}' + \mathbf{b}(\mathbf{x}, t), \tag{1.2}$$

where ρ is the mass density, $\mathbf{u}$ is the displacement field, $\hat{\mathbf{f}}$ is the force density whose value is the force vector (per unit volume squared) that the material point $\mathbf{x}'$ exerts on the material points $\mathbf{x}$, and $\mathbf{b}$ is a prescribed body force density field. Generally, the force density $\hat{\mathbf{f}}$ can be expressed as

$$\hat{\mathbf{f}}(\mathbf{x}, \mathbf{x}', t) = \underline{\mathbf{T}}[\mathbf{x}, t]\langle \boldsymbol{\xi} \rangle - \underline{\mathbf{T}}[\mathbf{x}', t]\langle -\boldsymbol{\xi} \rangle, \tag{1.3}$$

where $\underline{\mathbf{T}}$ is the force state field [6] which contains the information of the material constitutive behavior, and $\underline{\mathbf{T}}[\mathbf{x}, t]\langle \boldsymbol{\xi} \rangle$ denotes the force state at $\mathbf{x}$ and t, mapping the bond $\boldsymbol{\xi}$ to a force density. Based on Eq. (1.3), the balance of linear momentum can be satisfied by $\hat{\mathbf{f}}(\mathbf{x}, \mathbf{x}', t) = -\hat{\mathbf{f}}(\mathbf{x}', \mathbf{x}, t)$. According to the definition, the peridynamic models can be divided into two categories: bond-based and state-based [6], while state-based models can be further subdivided into ordinary state-based and non-ordinary state-based [8]. In ordinary state-based models, the force densities act in the direction of the corresponding bond

in the deformed configuration, but have unequal magnitudes. In non-ordinary state-based models, directions of the force densities are not restricted to be parallel to the deformed bond direction. Bond-based models are special cases of state-based model since their force density vector are equal in magnitude and also in the direction of the bond in the deformed configuration. For a static problem, the peridynamic equilibrium equation for $\mathbf{x} \in \Omega$ is written as

$$-\int_{\mathscr{H}(\mathbf{x},\delta)} \underline{\mathbf{T}}[\mathbf{x}]\langle \boldsymbol{\xi} \rangle - \underline{\mathbf{T}}[\mathbf{x}']\langle -\boldsymbol{\xi} \rangle d\mathbf{x}' = \mathbf{b}(\mathbf{x}) \tag{1.4}$$

In the peridynamic theory, it is common to assume that a material point $\mathbf{x} \in \Omega$ only interacts other points inside $\mathscr{H}(\mathbf{x}, \delta)$, as a result,

$$\underline{\mathbf{T}}[\mathbf{x}]\langle \boldsymbol{\xi} \rangle = 0 \quad \forall \mathbf{x}' \notin \mathscr{H}(\mathbf{x}, \delta). \tag{1.5}$$

In general, boundary conditions in peridynamics are imposed over a nonzero volumetric layer $\mathscr{B}\Omega \in \mathbb{R}^d$ surrounding the domain of interest $\Omega \subset \mathbb{R}^d$, which is different in the classical local problems based on PDEs, where boundary conditions are imposed over a lower-dimensional domain $\partial\Omega \in \mathbb{R}^{d-1}$. It thus leads to an entire problem domain $\overline{\overline{\Omega}} := \Omega \cup \mathscr{B}\Omega$. Typically, the width of $\mathscr{B}\Omega$ is δ for bond-based models and 2δ for state-based models [6].

1.3 Lennard-Jones model

The Lennard-Jones model (also termed the Lennard-Jones potential, LJ potential, 12-6 potential, or 6-12 potential) is a mathematical model that approximates the interatomic potential energy. Due to its simplicity, the model is commonly used to describe interactions

between neutral atoms or molecules or cyclic alkanes [15, 16]. It first emerged from Born's treatise on lattice enthalpies [17] and was elaborated by Lennard-Jones [18] in 1924. In general, the LJ potential of two particles, as shown in Fig. 1.1, can be expressed as:

$$\phi_{LJ}(r) = \phi_{rep}(r) + \phi_{att}(r) = 4\epsilon\left[(\frac{\sigma}{r})^{12} - (\frac{\sigma}{r})^{6}\right] = \epsilon\left[(\frac{r_m}{r})^{12} - 2(\frac{r_m}{r})^{6}\right] \tag{1.6}$$

where r is the distance between the particles, ϵ is the depth of the potential well, σ is the finite distance where the potential is zero, r_m is the finite distance where the potential reach its minimum, i.e. $\phi_{LJ}(r_m = 2^{1/6}\sigma) = -\epsilon$. As shown in Eq. (1.6), LJ potential consists of a repulsive term $\phi_{rep}(r)$ and an attractive term $\phi_{att}(r)$. The r^{12} term, which is $\phi_{rep}(r)$, represents the Pauli repulsion cased by overlapping electron orbitals, and the r^6 term, which is the smoother $\phi_{att}(r)$, represents the long-range attraction (dispersion force).

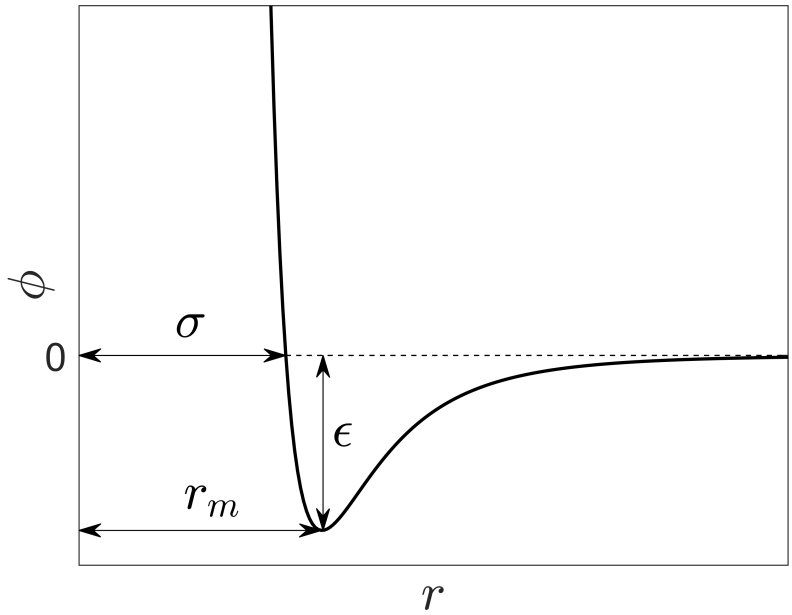

Figure 1.1: Lennard-Jones potential $\phi(r)$

Due the computational simplicity and interpretability, the LJ model is used extensively in computer simulations, and its parameters are determined to reproduce experimental data of particles interactions. There are also some limitations of such a simple model. Since it only has two parameters (ϵ and σ), the accuracy of approximating properties of a given real material is limited. In addition, when one particle approaches to another particle, the LJ potential diverges, which brings the requirement of special treatment in the computer simulation.

1.4 Outline of the thesis

The remainder of this thesis is organized as follows. Chapter 2 reviews two methods for the approximation of fields, the finite element method and the isogeometric analysis with a software framework, FEniCS. The Gaussian quadrature, the Riemann sum and the GMLS-based quadrature, which are used in the thesis, are introduced in Chapter 3. Chapter 4 studies the performance of GMLS-based quadrature method on weak form Peridynamics. Both 1D and 2D problem are considered in the Chapter 4. In Chapter 5, continuum models are built to simulate nonlocal interactions governed by the LJ potential in atomistic systems consisting of a monolayer MoS_2 and a multihole Si_3N_4 substrate. A simplified low-dimensional model is first investigated before the realistic higher-dimensional problem. Lastly, a conclusion of the thesis is given in Chapter 6.

Chapter 2

Different approximation methods of fields

2.1 Finite element method

Partial differential equations (PDEs) are usually used to describe physic laws for space- and time-dependent problems, such as heat transfer, fluid dynamics and elasticity. But for the majority of complex geometries and problems, their PDEs cannot be solved analytically, thus numerical methods need to be employed to approximate the solutions. The finite element method (FEM) is a widely used method that solves PDEs numerically and its approximation minimizes the associated error, which is referred to as the best approximation property [19]. Finite element analysis (FEA), as a practical application of FEM, is a computational tool for engineering analysis. Many well-known commercial software packages, such as ABAQUS, ANSYS, FEniCS, etc., provide user-friendly access to FEA

and develop a wide range of simulation options for varieties of engineering problems.

The general procedure of FEM based on the Bubnov–Galerkin method [19] is briefly reviewed by the solution of a simple 1D two-point boundary-value problem (BVP). The strong form of the problem is stated as follow: Given $f : \Omega \to \mathbb{R}$ and constants g and h, find $u : \overline{\Omega} \to \mathbb{R}$, such that

$$\begin{cases} u_{,xx} + f = 0, \quad \text{for } \mathbf{x} \in \Omega \\ u(1) = g, \\ -u_{,x}(0) = h, \end{cases} \tag{2.1}$$

where $\overline{\Omega} = [0, 1]$ (closed interval), $\Omega =]0, 1[$ (open interval), and the last two equation in 2.1 are Dirichlet and Neumann boundary conditions (BC), respectively. Then the weak form, as the counterpart of the strong form, is derived for the approximation purpose: Given f, g, h, as before, find $u \in \mathcal{S}$ such that $\forall\ v \in \mathcal{V}$

$$\int_0^1 u_{,x} v_{,x} dx = \int_0^1 f v dx + v(0)h, \tag{2.2}$$

where $\mathcal{S} = \{u | u \in H^1,\ u(1) = g\}$, $\mathcal{V} = \{v | v \in H^1,\ v(1) = 0\}$ and u and v are referred to as the trial and test functions, respectively. The equivalence of strong and weak forms is proved in [19]. The derivation of the weak form, which involves integration by parts, is omitted in this section for simplicity. Then based on the Bubnov–Galerkin method, the Galerkin form of the problem is stated as follows: Given f, g, h, as before, find $u^h \in \mathcal{S}^h$ such that $\forall\ v^h \in \mathcal{V}^h$

$$\int_0^1 u^h_{,x} v^h_{,x} dx = \int_0^1 f v^h dx + v^h(0)h, \tag{2.3}$$

where $\mathcal{S}^h \subset \mathcal{S}$ and $\mathcal{V}^h \subset \mathcal{V}$, which are finite-dimensional approximations. The superscript h denotes that $\mathcal{S}^h$ and $\mathcal{V}^h$ are associated with a mesh, or discretization, of Ω, which is

parameterized by a characteristic length scale h. In another word, h is the element size of the mesh with n elements. u^h and v^h are approximations of u and v, respectively, and are defined as:

$$v^h = \sum_{I=1}^{n_{int}} N_I c_I \tag{2.4}$$

$$u^h = v^h + g^h \tag{2.5}$$

where n_{int} is the number of nodes in Ω, d_I and c_I are constants, N_I is the shape function at node I, $g^h = gN_{n_{int}+1}$ (note that $x_{n_{int}+1} = 1$). Shape functions are required to have the Kronecker delta property for satisfying the approximation. The Galerkin form leads to the matrix form that finalized FEM procedure: Give the coefficient matrix $\mathbf{A}$ (stiffness matrix) and vector $\mathbf{F}$ (force vector), find $\mathbf{d}$ (displacement vector) such that

$$\mathbf{Ad} = \mathbf{F} \tag{2.6}$$

where

$$\mathbf{A} = [A_{IJ}] = [\int_0^1 N_{I,x} N_{J,x} dx], \tag{2.7}$$

$$\mathbf{F} = \{F_I\} = \{\int_0^1 N_I f dx + N_I(0)h - g\int_0^1 N_{I,x} N_{n_{int}+1,x} dx\}, \tag{2.8}$$

$$\mathbf{d} = \{d_J\}, \tag{2.9}$$

and $I,\ J = 1, 2, ..., n_{int}$. The solution of the matrix form is $\mathbf{d} = \mathbf{A}^{-1}\mathbf{F}$ which leads to the FEM solution as defined in Eq. (2.5). In this thesis, FEM is mainly used to solve problems in Chapter 4.

2.2 Isogeometric analysis with FEniCS

Isogeometric analysis (IGA) [20, 21] is a computational approach that integrates finite element analysis (FEA) with computer-aided design (CAD). Since the representations of geometry used in CAD and traditional FEA are different, a model conversion is necessary if the model created in a CAD program needs to be analyzed by FEA-based computer-aided engineering (CAE). In order to convert the model, the geometry needs to be designed in an analysis-suitable way in the first place and then approximated by a mesh of finite elements, which requires about 80% of overall analysis time [21]. Apart from the time cost, the mesh of finite elements brings additional errors to the analysis since it is only an approximation of the exact CAD geometry. Based on the above motivations, IGA was proposed by Hughes et al [20] in 2005. The idea of this technique is to unify the representations of geometry in CAD and FEA, by approximating the solution field with functions used to describe geometry in CAD, i.e. splines. By this, the mesh generation can be omitted and there is only one model needs to be designed and analyzed in stead of two. Moreover, there is no geometric approximation error in IGA since the domain is represented exactly. The CAD spline spaces also allow higher smoothness than traditional finite element function spaces. In the thesis, Chapter 5 takes advantage of the smoothness property to discretize the 4-th order Kirchhoff–Love shell model without needing to introduce rotational degrees of freedom.

FEniCS [22] is an open-source computing platform for solving partial differential equations (PDEs), and it was initiated in 2003 as an international research collaboration be-

tween institutions. The complexity of PDEs themselves may become a bottleneck in PDE-based analysis. To eliminate this bottleneck, FEniCS enables users to translate their scientific models into finite element code in an efficient and quick way: Specify variational formulations of PDEs by implementing a powerful Unified Form Language (UFL) [23]; compile the specified PDEs into efficient finite element routines [24] that are suitable for a multitude of platforms includes personal computers and high-performance clusters.

Both techniques (IGA and FEniCS) are efforts to explore ways of automating workflows for analysis based on PDEs, but with different premises as discussed above. In 2019, tIGAr, a prototype library, released by Kamensky and Bazilevs [25], first combines FEniCS's systematic approach to PDE-based analysis with the unification of CAD and FEA in IGA. The powerful library meets the need of engineers who consider increasingly-complex physical problems and aim to pose complex PDEs on geometries created in CAD programs. In this thesis, tIGAr is used as the main tool to solve problems explored in Chapter 5.

Chapter 3

Different quadrature schemes

For problems that involve complex integrals, especially for those with computer implementations, it may be costly or impossible to get analytical values for integrals. A numerical approximation of the integral, which is easier to be computed, can be applied for such dilemmas if it maintains enough accuracy for the problem. In this thesis, for instance, the FEM approximation of weak form peridynamics in Chapter 4 and the LJ energy integrated over a multi-hole substrate in Chapter 5 both need numerical approximations for the application purpose. Numerical quadrature (often abbreviated to quadrature), as a synonym for numerical integration, contains a variety of algorithms for the numerical approximation (value) of a definite integral. Generally, a quadrature scheme is stated as a weighted sum of function values at specified points, called quadrature points, within integration domain. This chapter introduces three quadrature schemes that are implemented in this thesis.

3.1 Gaussian quadrature

An n-point Gaussian quadrature rule is a popular quadrature scheme constructed to calculate an exact result for $2n-1$ (or less) degree polynomials. The locations of its quadrature points and associated weights are determined to achieve maximum accuracy, which makes the n-point Gaussian quadrature optimal in 1D with $2n$ order accuracy [19]. The most common integration interval for the Gaussian quadrature is $[-1,1]$, then the rule can be stated as:

$$\int_{-1}^{1} f(x)dx \approx \sum_{i=1}^{n} f(\xi_i)\omega_i, \tag{3.1}$$

where f is a smooth and integrable scalar function, ξ is the i-th quadrature points and ω_i is the associated weight. The rule accurately approximates $f(x)$ by polynomials and it will be exact if $f(x)$ is a polynomial of degree $2n-1$ or less. Tabulated values of ξ_i and ω_i can be found in [19] or many other public sources and conveniently accessed in some programming libraries for scientific computation, such as Numpy in Python which is broadly used in this thesis. For a practical application with an integral over $[a,b]$, the following relation needs to be applied for the interval change:

$$\begin{aligned}\int_{a}^{b} f(x)dx &= \frac{b-a}{2}\int_{-1}^{1} f(\frac{b-a}{2}\xi + \frac{a+b}{2}) \\ &\approx \frac{b-a}{2}\sum_{i=1}^{n} f(\frac{b-a}{2}\xi_i + \frac{a+b}{2})\omega_i.\end{aligned} \tag{3.2}$$

The Gaussian quadrature rule for integral in a higher dimension is constructed by employing the 1D rule stated above for each coordinate separately. For instance, the 2D rule for

a smooth and integrable function g is stated as:

$$\begin{aligned}\int_{-1}^{1}\int_{-1}^{1} g(\xi,\eta)d\xi d\eta &\approx \int_{-1}^{1}\Big\{\sum_{i=1}^{n^{(1)}} g(\xi_i^{(1)},\eta)\omega_i^{(1)}\Big\}d\eta \\ &\approx \sum_{j=1}^{n^{(2)}}\sum_{i=1}^{n^{(1)}} g(\xi_i^{(1)},\eta_j^{(2)})\omega_i^{(1)}\omega_j^{(2)}\end{aligned} \tag{3.3}$$

where superscripts stand for different 1D rules. To maintain accuracy, $n^{(1)}$ and $n^{(2)}$ are always chosen to be equivalent. In this thesis, Gaussian quadrature rules are mainly used in Chapter 4.

3.2 Riemann sum

The Riemann sum is another common quadrature scheme. The scheme calculates the integral of a scalar function f by approximating the function region using the sum of a finite number of simple shapes (partitions), e.g. rectangles, cubics, etc. A Riemann sum for a given 1D integral can be stated as:

$$\int_a^b f(x)dx = \lim_{\|\Delta x\|\to 0}\sum_{i=1}^{n} f(x_i^*)\Delta x_i^*, \tag{3.4}$$

where $a = x_0 < x_1 < x_2 < \cdots < x_n = b$, $\Delta x_i = x_i - x_{i-1}$ and $x_i^* \in [x_i, x_{i-1}]$, which implies the sum converges to the analytical integral result as the size of partitions goes to zero. Higher dimensional Riemann sum follows the same concept. For n dimensions, a Riemann sum can be stated as:

$$S^n = \sum_i f(P_i^*)\Delta V_i, \tag{3.5}$$

where V_i is a n-dimensional cell, ΔV_i is the associated n-dimensional volume and $P_i^* \in V_i$ is a point in the cell. In this thesis, the Riemann sum is mainly used in Chapter 4 and 5,

and refer to as the volume method for simplicity.

3.3 Quadrature rule based on GMLS

The method of Generalized Moving Least Squares (GMLS) is a non-parametric functional regression technique for constructing approximations, i.e. reconstructing functionals, by solving a collection of local least-squares problems based on scattered data points [26, 27, 28]. It can be used for data transfer between different meshes, and for meshless discretizations of differential problem.

In 2018, an asymptotically compatible meshfree quadrature rule based on GMLS for nonlocal problems was proposed by Trask et al [29]. The quadrature rule is presented in a form which may be applied to general nonlocal models beyond peridynamics, and its high-order convergence has been proved in [29]. The purpose of proposing the method is to seek a quadrature rule for a function $f \in \mathbf{V}$ of the form:

$$\int_{\mathscr{H}(\mathbf{x},\delta)} f d\mathbf{x}' = \sum_{j \in \mathbf{X}_q} f_j \omega_j, \tag{3.6}$$

where $\mathbf{X}_q = \{\mathbf{x}'_i\}_{i=1,\dots,N_q} \subset \mathscr{H}(\mathbf{x},\delta)$ is a collection of quadrature points excluding point $\mathbf{x}$, $\mathbf{V}$ is a function space, and $\{\omega_j\}$ is a collection of weights determined to exactly reproduce a finite dimensional subspace $\mathbf{V}_h \subset \mathbf{V}$. In peridynamics, the general form of f can be expressed as $K(\mathbf{x},\mathbf{x}')(u(\mathbf{x}') - u(\mathbf{x}))$, where u is the solution of the problem, e.g. for a bond-based peridynamic solid models, $u(\mathbf{x})$ is the displacement of $\mathbf{x}$ in the deformed configuration, and K is a kernel supported on the neighborhood $\mathscr{H}(\mathbf{x},\delta)$ of fixed $\mathbf{x}$ while $K(\mathbf{x},\mathbf{x}') = 0$ for $\mathbf{x}' \notin \mathscr{H}(\mathbf{x},\delta)$. It is common to assume that the kernel is radial, i.e.

$K(\mathbf{x}, \mathbf{x}') = K(\mathbf{x} - \mathbf{x}')$, and the kernel is thus singular as $\mathbf{x}' \to \mathbf{x}$.

Informally, Eq. (3.6) has a similar construction of the Gauss quadrature rule, where quadrature points and weights are selected to exactly reproduce polynomials. However, for many applications, there is no control over the location of quadrature points. Moreover, it is in general not possible to interpolate in unstructured data with dimension higher than one. A GMLS-based method, which has no location requirement for the points, is thus proposed to solve the problem. The weights are establish via a least squares problem subject to equality constraints to enforce reproduction as shown below:

$$\min_{\{\omega_j\}} \sum_j \omega_j^2 \quad \text{such that,} \quad I_h[p] = I[p] \quad \forall p \in \mathbf{V}_h \tag{3.7}$$

where $I[u]$ and $I_h[u]$ represent the quadrature functional and its approximation (Eq. (3.6)). For nonlocal problem, one should select $\mathbf{V}_h = P_m \cup S_{K,n,\mathbf{x}}$, where P_m is the space of m^{th}-order polynomials and

$$S_{K,n,\mathbf{x}} := \{K(\mathbf{x}, \mathbf{x}')f(\mathbf{x}') \,|\, f \in P_n\}. \tag{3.8}$$

In order to exactly reproduce $\mathbf{V}_h$, quadrature weights can be obtained from Eq. (3.7) by solving the following saddle-point problem:

$$\begin{bmatrix} \mathbf{I} & \mathbf{B}^T \\ \mathbf{B} & \mathbf{0} \end{bmatrix} \begin{bmatrix} \boldsymbol{\omega} \\ \boldsymbol{\lambda} \end{bmatrix} = \begin{bmatrix} \mathbf{0} \\ \mathbf{g} \end{bmatrix}, \tag{3.9}$$

where $\mathbf{I} \in \mathbb{R}^{N_q \times N_q}$ is the identity matrix, $\boldsymbol{w} \in \mathbb{R}^{N_q}$ is the set of quadrature weights, $\boldsymbol{\lambda} \in \mathbb{R}^{\dim(\mathbf{V}_h)}$ is a set of Lagrange multipliers for enforcing reproducability, $\mathbf{B} \in \mathbb{R}^{N_q \times \dim(\mathbf{V}_h)}$ is the reproducing set computed at each quadrature point (i.e. $B_{aj} = p^\alpha(\mathbf{x}_j)$, $\forall p^\alpha \in \mathbf{V}_h$), and $\mathbf{g} \in \mathbb{R}^{\dim(\mathbf{V}_h)}$ is the set of the integral of each function in the reproducing set over

$\mathscr{H}(\mathbf{x}, \delta)$ (i.e. $g^\alpha = I[p^\alpha]$). Based on Eq. (3.9), quadrature weights can be obtained by solving

$$\boldsymbol{\omega} = \mathbf{B}^{\mathrm{T}}\mathbf{S}^{-1}\mathbf{g}, \tag{3.10}$$

where $\mathbf{S} = \mathbf{B}\mathbf{B}^{\mathrm{T}}$. In the following chapters, pseudoinverse will be used to solve to problem when the reproducing constraints are redundant.

Chapter 4

Nonlocal interactions in weak form peridynamics

This chapter investigates the convergence behaviour of the GMLS-based quadrature rule applied on weak form peridynamics for one- and two-dimensional problems. The double integral in weak form peridynamics [30] is first introduced. Then for both dimensions, numerical results are shown after the problem and quadrature constructions.

Convergence in peridynamics : The concept of convergence in peridynamics is different from the convergence in traditional FEM due to the non-locality and the intrinsic length-scale determined by the horizon δ in peridynamics. Since the classical PDE has no length-scale, it's reasonable to consider $\delta \to 0$ for convergence studies in peridynamics. Given a uniform spatial discretization of $\overline{\overline{\Omega}}$ with spacing h so that $\delta/h = m \in \mathbb{R}_*^+$, the convergence in peridynamics can be defined in two types [31, 32]:

- The h-convergence: Fix δ and $h \to 0$. The approximation converges to the non-local peridynamics solution with horizon δ.
- The δ-convergence: $\delta \to 0$ and m is fixed or increases at a different rate compared with that of δ decrease. The approximation converges to the local classical solution.

For the numerical problems in this chapter, δ-convergence with fixed m is used to investigate properties of different quadrature schemes. For the convergence studies, the L^2 error norm of the numerical solution $\left\|u^h - u\right\|_2$ is considered, which is computed using Gaussian quadrature. The programming language for this chapter is Python.

4.1 The double integral in weak form peridynamics

4.1.1 The derivation of weak form peridynamics

To study the weak form peridynamics, a general nonlocal BVP in strong form is considered: Given $b : \Omega \to \mathbb{R}^d$ and g, find $u : \overline{\overline{\Omega}} \to \mathbb{R}^d$, such that

$$\begin{cases} -\displaystyle\int_{\mathscr{H}(\mathbf{x},\delta)} K(\mathbf{x},\mathbf{x}')(u(\mathbf{x}') - u(\mathbf{x}))d\mathbf{x}' = b(\mathbf{x}), \quad \text{for } \mathbf{x} \in \Omega \\ \\ u(\mathbf{x}) = g(\mathbf{x}), \quad \text{for } \mathbf{x} \in \mathscr{B}\Omega \end{cases} \tag{4.1}$$

where K is the kernel function, $b(\mathbf{x})$ is the body force density field (source term), $g(\mathbf{x})$ is a given function for Dirichlet boundary condition, $\mathscr{H}(\mathbf{x},\delta)$, $\overline{\overline{\Omega}}$, Ω and $\mathscr{B}\Omega$ are defined in Section 1.2 and $\mathbf{x} \in \mathscr{B}\Omega$ is the Dirichlet boundary. By multiplying the first equation in Eq. (4.1) by a test function $v(\mathbf{x})$ and leverage the nonlocal version of integration by parts [33], which is a usual manner from the traditional FEM as introduced in Section 2.1, the

weak form of Eq. (4.1) can be derived: Given b, g, as before, find $u \in \mathcal{S}$ such that $\forall\ v \in \mathcal{V}$

$$D(u, v) = G(v), \tag{4.2}$$

where

$$D(u, v) = \frac{1}{2} \int_{\overline{\Omega}} \int_{\mathscr{H}(\mathbf{x},\delta)\cap\overline{\Omega}} K(\mathbf{x}, \mathbf{x}')(u(\mathbf{x}') - u(\mathbf{x}))(v(\mathbf{x}') - v(\mathbf{x}))d\mathbf{x}'d\mathbf{x} \tag{4.3}$$

and

$$G(v) = \int_{\Omega} v(\mathbf{x})b(\mathbf{x})d\mathbf{x}. \tag{4.4}$$

where $\mathcal{S} = \{u|u \in H^0,\ u(\mathbf{x}) = g(\mathbf{x}) \text{ for } \mathbf{x} \in \mathscr{B}\Omega\}$, $\mathcal{V} = \{u|u \in H^0,\ u(\mathbf{x}) = 0 \text{ for } \mathbf{x} \in \mathscr{B}\Omega\}$. The double integral operator $\int(\int(\cdots)d\mathbf{x}')d\mathbf{x}$ thus appears in the weak form. $\int(\cdots)d\mathbf{x}'$ is referred to as the *inner integral* while $\int(\cdots)d\mathbf{x}$ is the *outer integral*.

4.1.2 FE approximation of the weak formulation

To solve the given nonlocal BVP, the FE Galerkin approximation needs to be formulated. Follow the general procedure introduced in Section 2.1, The Bubnov–Galerkin form of Eq. (4.2) can be obtained as: Given b, g, as before, find $u^h \in \mathcal{S}^h$ such that $\forall\ v^h \in \mathcal{V}^h$

$$D(u^h, v^h) = G(v^h), \tag{4.5}$$

where $\mathcal{S}^h \subset \mathcal{S}$ and $\mathcal{V}^h \subset \mathcal{V}$, u^h and v^h have similar definitions as stated in Eq. (2.5) and Eq. (2.4) while

$$g^h = \begin{cases} g(\mathbf{x}) & \text{for } \mathbf{x} \in \mathscr{B}\Omega, \\ 0 & \text{for } \mathbf{x} \in \Omega, \end{cases} \tag{4.6}$$

which leads to the following matrix form: Give the coefficient matrix $\mathbf{A}$ and vector $\mathbf{F}$, find $\mathbf{d}$ such that

$$\mathbf{A}\mathbf{d} = \mathbf{F}, \tag{4.7}$$

and the components of $\mathbf{A}$ and $\mathbf{F}$ are defined as:

$$A_{IJ} = D(N_I, N_J), \tag{4.8}$$

$$F_I = G(N_I) - D(N_I, g^h), \tag{4.9}$$

where N is FE shape function. In this thesis, the continuous linear shape function is used.

4.1.3 Quadrature for the weak formulation

Based on the FE approximation, the overall domain $\overline{\overline{\Omega}}$ is discretized into n_{el} elements Ω_{el} so that $\cup\Omega_{el} = \overline{\overline{\Omega}}$. Then for the study of quadrature schemes, the left-hand side (LHS) and right-hand side (RHS) of Eq. (4.2) are discretized as:

$$\begin{aligned}
D(u,v) &= \frac{1}{2}\int_{\overline{\overline{\Omega}}}\int_{\mathscr{H}(\mathbf{x},\delta)\cap\overline{\overline{\Omega}}} K(\mathbf{x},\mathbf{x}')(u(\mathbf{x}')-u(\mathbf{x}))(v(\mathbf{x}')-v(\mathbf{x}))d\mathbf{x}'d\mathbf{x} \\
&= \frac{1}{2}\sum_{n_{el}}\int_{\Omega_{el}}\int_{\mathscr{H}(\mathbf{x},\delta)\cap\overline{\overline{\Omega}}} K(\mathbf{x},\mathbf{x}')(u(\mathbf{x}')-u(\mathbf{x}))(v(\mathbf{x}')-v(\mathbf{x}))d\mathbf{x}'d\mathbf{x} \\
&\approx \frac{1}{2}\sum_{n_{el}}\sum_{Q}\int_{\mathscr{H}(\mathbf{x},\delta)\cap\overline{\overline{\Omega}}} K(\mathbf{x}^{\mathbf{Q}},\mathbf{x}')(u(\mathbf{x}')-u(\mathbf{x}^{\mathbf{Q}}))(v(\mathbf{x}')-v(\mathbf{x}^{\mathbf{Q}}))d\mathbf{x}'V^Q \\
&\approx \frac{1}{2}\sum_{n_{el}}\sum_{Q}\sum_{P} K(\mathbf{x}^{\mathbf{Q}},\mathbf{x}^{\mathbf{P}})(u(\mathbf{x}^{\mathbf{P}})-u(\mathbf{x}^{\mathbf{Q}}))(v(\mathbf{x}^{\mathbf{P}})-v(\mathbf{x}^{\mathbf{Q}}))V^PV^Q \\
&= D_h(u,v)
\end{aligned} \tag{4.10}$$

and

$$
\begin{aligned}
G(v) &= \int_{\Omega} v(\mathbf{x}) b(\mathbf{x}) d\mathbf{x} \\
&= \sum_{n_{el}} \int_{\Omega_{el}} v(\mathbf{x}) b(\mathbf{x}) d\mathbf{x} \\
&\approx \sum_{n_{el}} \sum_{G} v(\mathbf{x}^{\mathbf{G}}) b(\mathbf{x}^{\mathbf{G}}) V^{G} \\
&= G_h(v)
\end{aligned}
\tag{4.11}
$$

where $\mathbf{x}^{\mathbf{Q}}$ and $\mathbf{x}^{\mathbf{P}}$ are quadrature points for outer and inner integral, respectively, V^Q and V^P are the corresponding quadrature weight. $\mathbf{x}^{\mathbf{G}}$ and V^G are used for the quadrature of LHS and they are not necessarily identical to those for outer integrals of RHS. The approximation from the second to the third equation of Eq. (4.10) refers to as the *outer quadrature*, while the third to the fourth equation refers to as the *inner quadrature*. In this chapter, a 12-points Gaussian quadrature rule is used for RHS, while the GMLS-based quadrature is leveraged for LHS. The exact $b(\mathbf{x})$ is used without FE approximations.

4.2 One-dimensional problem

4.2.1 1D problem construction

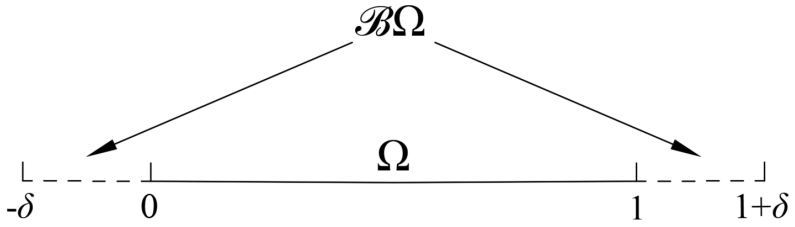

Figure 4.1: 1D domain $\overline{\overline{\Omega}} = \Omega \cup \mathscr{B}\Omega$

For convergence studies, the inner solution domain Ω needs to be consistent during the refinement ($\delta \to 0$) so that the associated L_2 error norm is comparable. In this section, the one-dimensional problem domain is defined as an inner domain $\Omega = (0, 1)$ with the boundary layer $\mathscr{B}\Omega = [-\delta, 0] \cup [1, \delta]$, which builds the entire domain $\overline{\overline{\Omega}} = \Omega \cup \mathscr{B}\Omega = [-\delta, 1 + \delta]$. The 1D kernel function K is defined as follow:

$$K(x', x) = c_1 \omega_1(|\xi|) \tag{4.12}$$

where c_1 is the 1D constitutive constant, ω_1 is a 1D influence function and $\xi = x' - x$. An influence function [6] is a scalar function that is used to weight the force state with a finite support depends on δ. Two types of influence functions with $c_1 = 2$ are considered [34]:

$$\omega_{1,r}(|\xi|) = \begin{cases} \dfrac{1}{\delta^2 |\xi|} & \text{for } |\xi| \leq \delta, \\ 0 & \text{for } |\xi| > \delta, \end{cases} \tag{4.13}$$

and

$$\omega_{1,c}(|\xi|) = \begin{cases} \dfrac{3}{2\delta^3} & \text{for } |\xi| \leq \delta, \\ 0 & \text{for } |\xi| > \delta, \end{cases} \tag{4.14}$$

where $\omega_{1,r}$ is the rational influence function that depends on $|\xi|$ and $\omega_{1,c}$ is the constant influence function. For the convergence study, a sinusoidal function $u(x) = \sin 2\pi x$ is considered as the manufactured solution. Since the chosen δ-convergence is based on the local solution, the body force density is calculated as:

$$\begin{aligned} b(x) &= -\Delta u(x) \\ &= -\Delta \sin 2\pi x \\ &= 4\pi^2 \sin 2\pi x \end{aligned} \tag{4.15}$$

4.2.2 1D GMLS-based quadrature construction

The GMLS-based quadrature construction follows Section 3.3, which makes the coefficient of the integral ($\frac{1}{2}$ in this case) ignorable. u and v are approximated by the linear space (i.e. $u(x) = x$ and $v(x) = x$). Consider an element $\Omega_{el} = [x_l, x_r] \subset \Omega$ with N_q outer quadrature points, and the q-th outer quadrature point x_q^Q has a 1D neighborhood $\mathscr{H}(x_q^Q, \delta) = [x_q^Q - \delta, x_q^Q + \delta]$ with N_{qp} inner quadrature points (neighbor points of x_q^Q), then the inner quadrature for x_q^Q is built as:

$$\int_{x_q^Q-\delta}^{x_q^Q+\delta} c_1\omega_1(x_q^Q, x')(x' - x_q^Q)(x' - x_q^Q)dx' = \sum_{p=1}^{N_{qp}} c_1\omega_1(x_q^Q, x_{qp}^P)(x_{qp}^P - x_q^Q)(x_{qp}^P - x_q^Q)V_{qp}^P \tag{4.16}$$

where x_{qp}^P is the p-th neighbor points of x_q^Q and V_{qp}^P is the associated weight. According to Eq. (3.10), the inner weight vector $\mathbf{V_q^P}$ can thus be calculated as:

$$\mathbf{V_q^P} = \mathbf{B_q^{in}}^{\mathrm{T}} {S_q^{in}}^{-1} g_q^{in}, \tag{4.17}$$

where

$$g_q^{in} = \int_{x_q^Q-\delta}^{x_q^Q+\delta} c_1\omega_1(x_q^Q, x')(x' - x_q^Q)(x' - x_q^Q)dx', \tag{4.18}$$

$$[B_q^{in}]_p = c_1\omega_1(x_q^Q, x_{qp}^P)(x_{qp}^P - x_q^Q)(x_{qp}^P - x_q^Q), \tag{4.19}$$

and $S_q^{in} = \mathbf{B_q^{in}}\mathbf{B_q^{in}}^{\mathrm{T}}$. $\mathbf{S}$ and $\mathbf{g}$ reduce to constants since $\mathbf{B_q^{in}}$ is a $1 \times n_{qp}$ vector. Then the outer quadrature for the element Ω_{el} can be built as:

$$\int_{x_l}^{x_r} \int_{x-\delta}^{x+\delta} c_1\omega_1(x, x')(x' - x)(x' - x)dx'dx = \sum_{q=1}^{N_q} g_q^{in} V_q^Q. \tag{4.20}$$

Then the outer weight vector $\mathbf{V^Q}$ can be calculated as:

$$\mathbf{V^Q} = \mathbf{B^{out}}^{\mathrm{T}} {S^{out}}^{-1} g^{out}, \tag{4.21}$$

where

$$g^{out} = \int_{x_l}^{x_r} \int_{x-\delta}^{x+\delta} c_1 \omega_1(x, x')(x' - x)(x' - x) dx' dx, \tag{4.22}$$

$$[B^{out}]_q = g_q^{in}, \tag{4.23}$$

and $S^{out} = \mathbf{B^{out}} \mathbf{B^{out}}^{\mathrm{T}}$. Again, $\mathbf{S}$ and $\mathbf{g}$ reduce to constants since $\mathbf{B^{out}}$ is a $1 \times n_q$ vector. The components of $\mathbf{B^{out}}$ can be also obtained by the inner quadrature derived above which is constructed to be exact for the chosen basis.

While the outer quadrature points are uniformly placed in each element, this thesis considers two different schemes for the placement of inner quadrature points, as shown in Fig. 4.2. For an arbitrary outer quadrature point Q (red circle), the element-based method simply chooses the existent outer quadrature points which belong to $\mathscr{H}(Q, \delta)$ as the inner quadrature points, which only needs to discretized $\overline{\overline{\Omega}}$ once. The ball-based method places N_{qp} inner quadrature points uniformly and symmetrically within $\mathscr{H}(Q, \delta)$ regardless of the existent points. The ball-based method allows different discretizations in $\mathscr{H}(Q, \delta)$ while the uniformity and symmetry can be maintained when the discretization of $\overline{\overline{\Omega}}$ is non-uniform. However, if $Q \in \mathscr{B}\Omega$, the integration over the $\mathscr{H}(Q, \delta)$ will be cut off by the edge of $\overline{\overline{\Omega}}$ as shown in Fig. 4.3. In this case, the inner quadrature is asymmetrical respect to Q, which may introduce additional error to the solution. To resolve this issue, the inner quadrature can be constructed over the full neighbourhood for symmetry. An extension of the mesh is considered in the numerical test so that quadrature points can exist outside $\overline{\overline{\Omega}}$, mainly for the element-based method. The extension size t_e needs to be larger than or equal to δ.

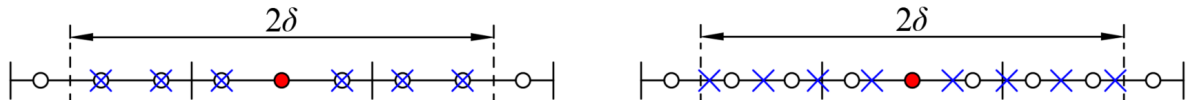

(a) Element-based (b) Ball-based

Figure 4.2: Considered schemes for the placement of quadrature points 1D. Outer quadrature points are indicated by circles; inner quadrature points are represented by crosses.

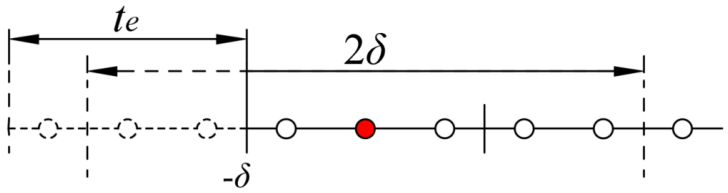

Figure 4.3: The reduced inner integration interval of the red point ($[-\delta, Q+\delta]$) and a mesh extension with size t_e

4.2.3 Numerical results for uniform discretizations

In this subsection, the convergence behaviour of GMLS-based quadrature on uniform discretizations is investigated. For the δ-convergence study, m is chosen as 2 or 3. Both $\omega_{1,r}$ and $\omega_{1,c}$ are considered in the numerical tests. The mesh is built uniformly over $[-\delta, 1+\delta]$ with spacing h and then N_q outer quadrature points are uniformly placed in each element, and $N_q = 5$ for all elements. When the extension of the mesh is introduced, the mesh domain becomes $[-\delta - t_e, 1+\delta+t_e]$, and $t_e = \delta$ is used in this thesis. For simplicity, the mesh without extension is annotated as $t_e = 0$. While for the element-based method, N_{qp} depends on m and the position of the outer quadrature point (if $t_e = 0$), the N_{qp}

of the ball-based method is chosen to be 14 (if no truncation). The numerical results presented in Fig. 4.5 and Fig. 4.6 show that GMLS-based method converges for the given influence functions and different m. The convergence rate of $t_e = \delta$ method is 2, while the $t_e = 0$ cases only show first-order convergence. The larger error of $t_e = 0$ is expected as discussed in the previous subsection. Fig. 4.4 shows that the error of $t_e = 0$ is significant at the region near $\mathscr{B}\Omega$, which implies the first-order convergence behaviour is dominated by the refinement of the boundary layer. When the mesh is extended, the large boundary effect is eliminated by the global symmetrical inner quadrature. Considering the decent property of the mesh extension, the remaining sections in this chapter mainly used $t_e = \delta$ for numerical tests.

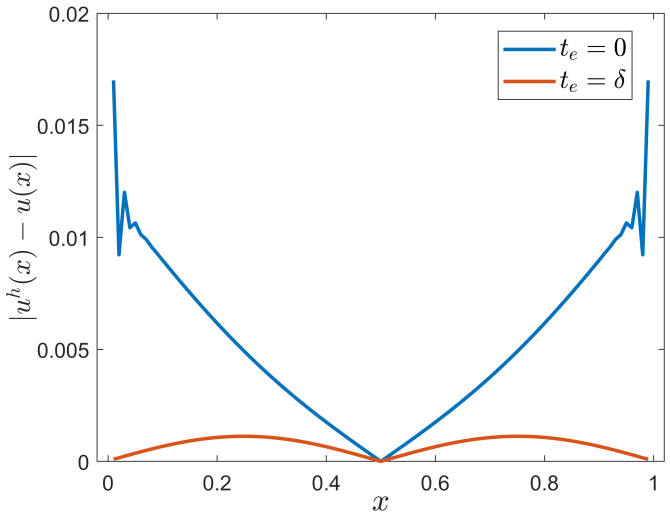

Figure 4.4: Comparison of $|u^h(x) - u(x)|$ over Ω with $t_e = 0$ and $t_e = \delta$. Ball-based method, $m = 2$, $h = 0.01$ and $\omega_{1,r}$ are used for this test.

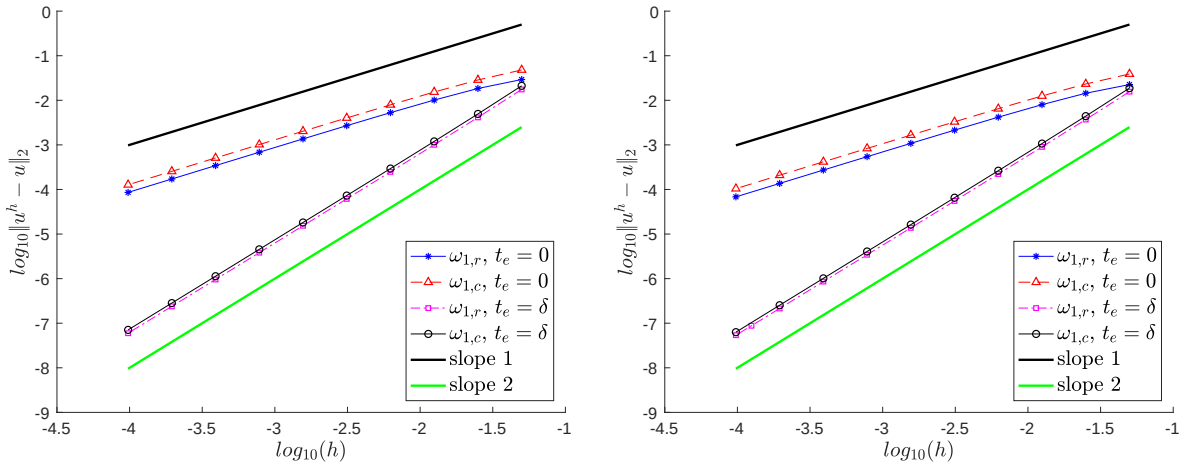

(a) Element-based (b) Ball-based

Figure 4.5: Convergence behaviours for the 1D sinusoidal exact solution. $m = 2$. Uniform discretization. $t_e = 0$ and $t_e = \delta$ are both considered.

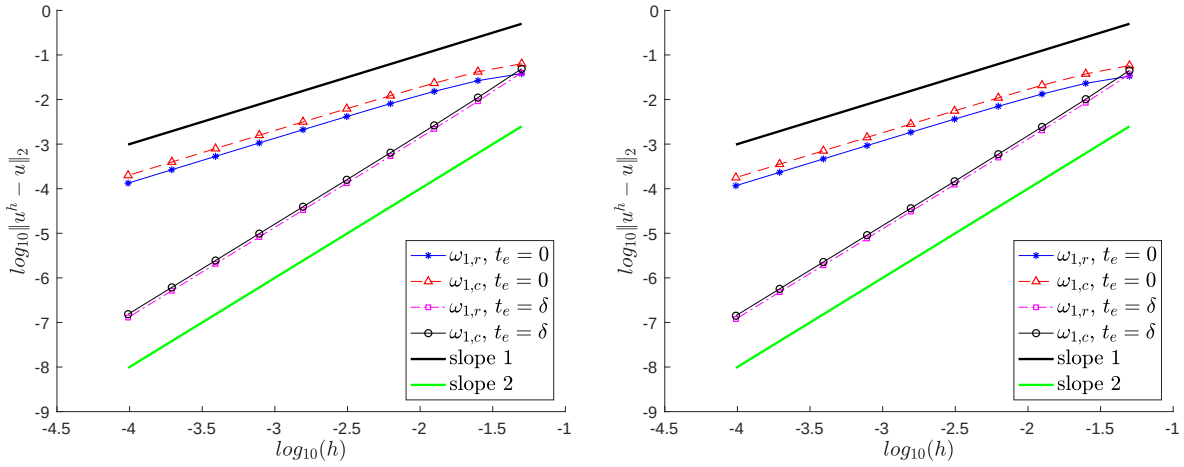

(a) Element-based (b) Ball-based

Figure 4.6: Convergence behaviours for the 1D sinusoidal exact solution. $m = 3$. Uniform discretization. $t_e = 0$ and $t_e = \delta$ are both considered.

4.2.4 Numerical results for non-uniform discretizations

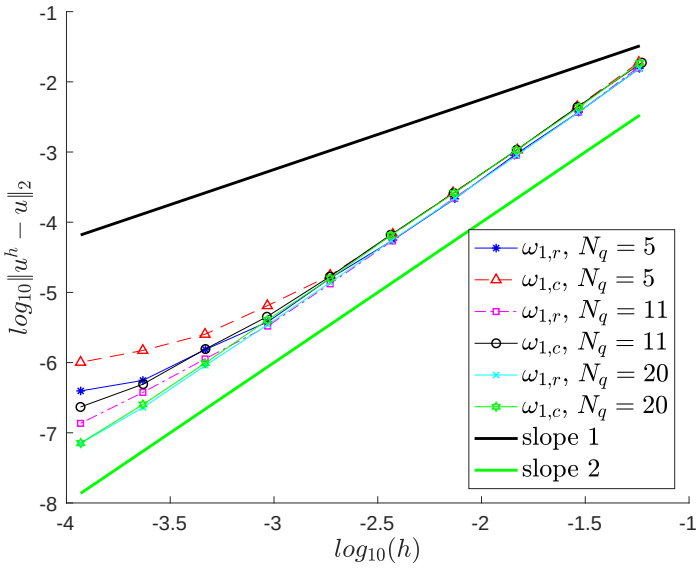

Figure 4.7: Convergence behaviours for the 1D sinusoidal exact solution using ball-based method. Non-uniform discretization with $\epsilon = 0.1$. $m = 2$ and $t_e = \delta$.

To study the robustness of the method, the convergence behaviour of GMLS-based quadrature on non-uniform discretizations is investigated. The discretization is first built uniformly. Then a perturbation is added to the edges of each element while keeping the edges of Ω fixed. The perturbation is given as $\epsilon h R_a$, where ϵ is the perturbation factor, h is the size of the uniform discretization and R_a is a random number ranges from -1 to 1. ϵ is chosen as 0.1 for the following numerical tests. After introducing perturbations to the mesh, the outer quadrature points are still placed in each element uniformly. The element-based method does not converge for the non-uniform discretization since the symmetry in the inner quadrature is destroyed by perturbations, while the ball-based method can maintain a symmetrical inner quadrature. Fig. 4.7 shows that the convergence rate

decreases when $log_{10}(h) < -3$. The plateau behaviour can be improved by increasing the number of outer quadrature, i.e. a larger N_q leads to a better convergence behaviour, which is reasonable considering the complex nature of the weak form peridynamics. To further study the concept of increasing N_q, similar numerical tests are accomplished for the monomial exact solution (x^2 and x^3). As shown in Fig. 4.8 and Fig. 4.9, the plateau behaviour is even more obvious for monimials with small N_q, and the influence of increasing N_q is consistent with the previous test.

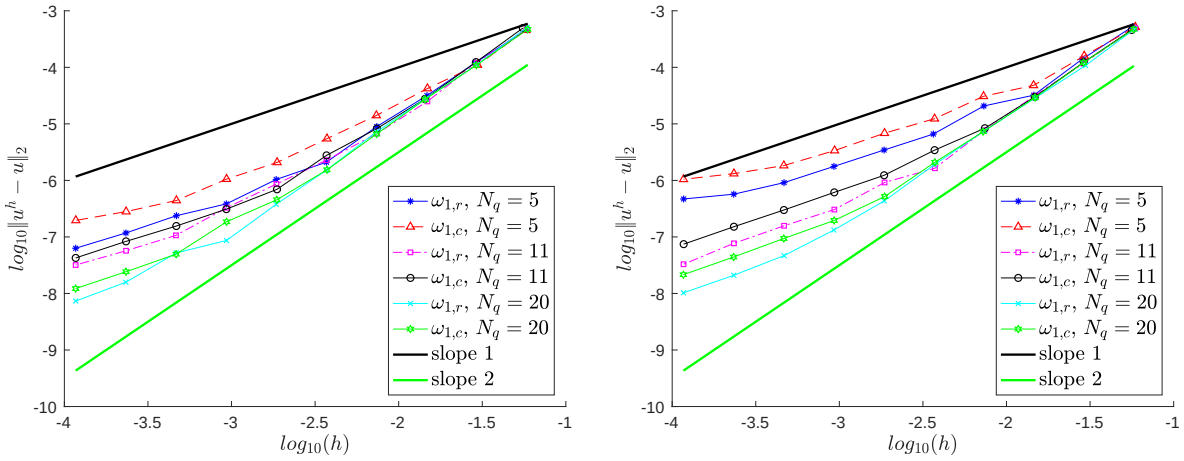

(a) $m = 2$ (b) $m = 3$

Figure 4.8: Convergence behaviours for the 1D second-order monomial (x^2) exact solution using ball-based method. Non-uniform discretization with $\epsilon = 0.1$. $t_e = \delta$.

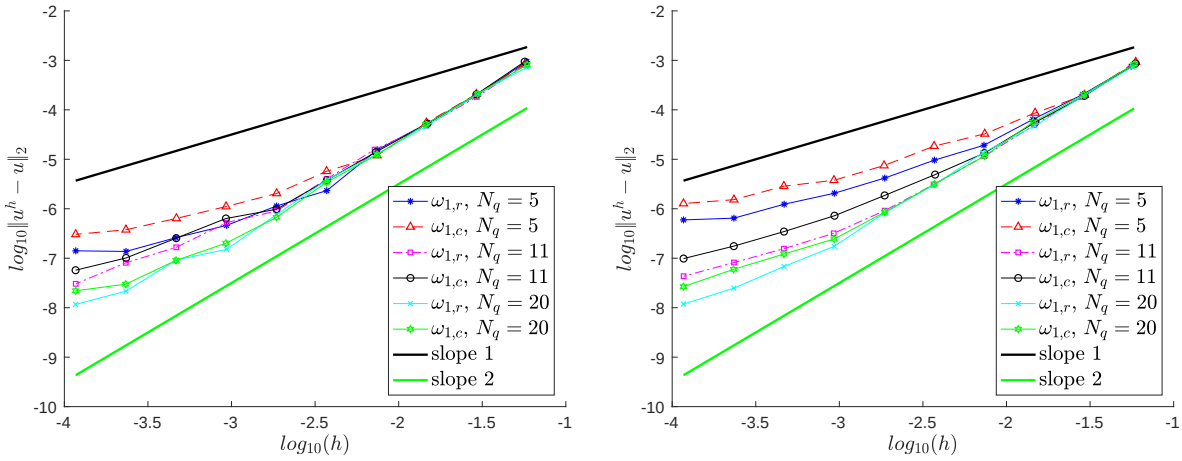

(a) $m = 2$ (b) $m = 3$

Figure 4.9: Convergence behaviours for the 1D third-order monomial (x^3) exact solution using ball-based method. Non-uniform discretization with $\epsilon = 0.1$. $t_e = \delta$.

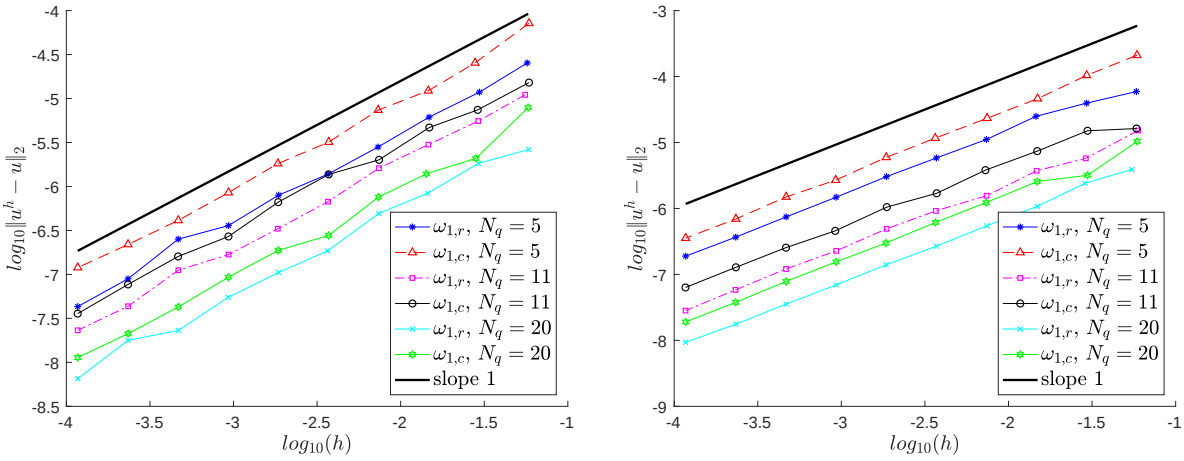

(a) $m = 2$ (b) $m = 3$

Figure 4.10: Convergence behaviours for the 1D first-order monomial (x) exact solution using ball-based method. Non-uniform discretization with $\epsilon = 0.1$. $t_e = \delta$.

However, the numerical tests for the first-order monomial (x) show first-order convergence, but with lower error norm compared with other exact solutions. Considering the Taylor series, this observation implies the convergence of the sinusoidal solution may eventually decay to the first-order. While the GMLS-based method preserves linear consistency in the uniform case, the behavior shown in non-uniform tests is a useful hint for error analysis in the future.

4.3 Two-dimensional problem

4.3.1 2D problem construction

In this section, the two-dimensional problem domain is defined as an inner domain $\Omega = (0,1)\times(0,1)$ with the boundary layer $\mathscr{B}\Omega = \overline{\overline{\Omega}}\setminus\Omega$, where $\overline{\overline{\Omega}} = \{\mathbf{x}' \in \mathbb{R}^2 : \|\boldsymbol{\xi}\| \leq \delta, \forall \mathbf{x} \in \Omega\}$ and $\boldsymbol{\xi} = \mathbf{x}' - \mathbf{x}$. The 2D kernel function K is defined as follow:

$$K(\mathbf{x}', \mathbf{x}) = c_2 \omega_2(\|\boldsymbol{\xi}\|) \tag{4.24}$$

where c_2 is the 2D constitutive constant and ω_2 is a 2D influence function. Two types of influence functions with $c_2 = 2$ are considered [34]:

$$\omega_{2,r}(\|\boldsymbol{\xi}\|) = \begin{cases} \dfrac{3}{\pi\delta^3\|\boldsymbol{\xi}\|} & \text{for } \|\boldsymbol{\xi}\| \leq \delta, \\ 0 & \text{for } \|\boldsymbol{\xi}\| > \delta, \end{cases} \tag{4.25}$$

and

$$\omega_{2,c}(\|\boldsymbol{\xi}\|) = \begin{cases} \dfrac{4}{\pi\delta^4} & \text{for } \|\boldsymbol{\xi}\| \leq \delta, \\ 0 & \text{for } \|\boldsymbol{\xi}\| > \delta, \end{cases} \tag{4.26}$$

where $\omega_{2,r}$ is the 2D rational influence function that depends on $\|\boldsymbol{\xi}\|$ and $\omega_{2,c}$ the 2D constant influence function. Again, a sinusoidal function $u(\mathbf{x}) = \sin 2\pi x_1 \cdot \sin 2\pi x_2$ is considered as the manufactured solution. The body force density is calculated as:

$$\begin{aligned} b(\mathbf{x}) &= -\Delta u(\mathbf{x}) \\ &= -\Delta(\sin 2\pi x_1 \cdot \sin 2\pi x_2) \\ &= 8\pi^2 \sin 2\pi x_1 \cdot \sin 2\pi x_2 \end{aligned} \tag{4.27}$$

4.3.2 2D GMLS-based quadrature construction

To be consistent with 1D quadrature, u and v are approximated by the linear space (i.e. $u(\mathbf{x}) = x_1$ or x_2, $v(\mathbf{x}) = x_1$ or x_2). Consider an element $\Omega_{el} \subset \Omega$ with N_q outer quadrature points, and the q-th outer quadrature point $\mathbf{x_q^Q}$ has a 2D spherical neighborhood $\mathscr{H}(\mathbf{x_q^Q}, \delta)$ with N_{qp} inner quadrature points (neighbor points of $\mathbf{x_q^Q}$), then the inner quadrature for $\mathbf{x_q^Q}$ is built as:

$$\int_{\mathscr{H}(\mathbf{x}_q^Q,\delta)} c_2\omega_2(\|\boldsymbol{\xi}_q\|)p_n(\mathbf{x}', \mathbf{x}_q^Q)d\mathbf{x}' = \sum_{p=1}^{N_{qp}} c_2\omega_2(\|\boldsymbol{\xi}_{qp}\|)p_n(\mathbf{x}_{qp}^P, \mathbf{x}_q^Q)V_{qp}^P \tag{4.28}$$

where $\boldsymbol{\xi}_q = \mathbf{x}' - \mathbf{x}_q^Q$, $\boldsymbol{\xi}_{qp} = \mathbf{x}_{qp}^P - \mathbf{x}_q^Q$ and

$$\begin{cases} p_1(\mathbf{x}', \mathbf{x}) = (x'_1 - x_1)(x'_1 - x_1), \\ p_2(\mathbf{x}', \mathbf{x}) = (x'_2 - x_2)(x'_1 - x_1), \\ p_3(\mathbf{x}', \mathbf{x}) = (x'_2 - x_2)(x'_2 - x_2), \end{cases} \tag{4.29}$$

The quadrature is constructed for the all the p_n $(n = 1, 2, 3)$ above that are based on all the possible combination of linear u and v.

$$\mathbf{V_q^P} = \mathbf{B_q^{in}}^{\mathrm{T}} \mathbf{S_q^{in}}^{-1} \mathbf{g_q^{in}}, \tag{4.30}$$

where $\mathbf{S^{in}} = \mathbf{B^{in}}\mathbf{B^{in}}^{\mathrm{T}}$, $\mathbf{B_q^{in}}$ is a $3 \times n_{qp}$ matrix, $\mathbf{g_q^{in}}$ is a 3×1 vector and their components are given as:

$$[g_q^{in}]_n = \int_{\mathscr{H}(\mathbf{x}_q^Q,\delta)} c_2\omega_2(\|\boldsymbol{\xi}_q\|)p_n(\mathbf{x}', \mathbf{x}_q^Q)d\mathbf{x}' \tag{4.31}$$

$$[B_q^{in}]_{np} = c_2\omega_2(\|\boldsymbol{\xi}_{qp}\|)p_n(\mathbf{x}_{qp}^P, \mathbf{x}_q^Q) \tag{4.32}$$

Then the outer quadrature is stated as:

$$\int_{\Omega_{el}} \int_{\mathscr{H}(\mathbf{x}_q^Q,\delta)} c_2\omega_2(\|\boldsymbol{\xi}\|)p_n(\mathbf{x}', \mathbf{x})d\mathbf{x}'d\mathbf{x} = \sum_{q=1}^{N_q} [g_q^{in}]_n V_q^Q \tag{4.33}$$

Then the outer weight vector $\mathbf{V^Q}$ can be calculated as:

$$\mathbf{V^Q} = \mathbf{B^{out}}^{\mathrm{T}}\mathbf{S^{out}}^{-1}\mathbf{g^{out}}, \tag{4.34}$$

where $\mathbf{S^{out}} = \mathbf{B^{out}}\mathbf{B^{out}}^{\mathrm{T}}$, $\mathbf{B^{out}}$ is a $3\times n_q$ matrix, $\mathbf{g^{out}}$ is a 3×1 vector and their components are given as:

$$[g^{out}]_n = \int_{\Omega_{el}} \int_{\mathscr{H}(\mathbf{x}_q^Q,\delta)} c_2\omega_2(\|\boldsymbol{\xi}\|)p_n(\mathbf{x}', \mathbf{x})d\mathbf{x}'d\mathbf{x} \tag{4.35}$$

$$[B^{out}]_{nq} = [g_q^{in}]_n, \tag{4.36}$$

Same as 1D, the Element-based and Ball-based method are considered for the placement of inner quadrature points, as shown in Fig. 4.11. For the symmetry in the ball-based method, $\bar{N}_{qp}$ points are first placed uniformly over a square around the red point Q, then choose the points in $\mathscr{H}(\mathbf{Q}, \delta)$ as the inner quadrature points ($N_{qp} < \bar{N}_{qp}$). If an outer quadrature point $Q \in \mathscr{B}\Omega$, its inner quadrature will still be asymmetrical as shown in Fig. 4.12. The mesh extension is thus considered with size t_e as discussed in 1D problem.

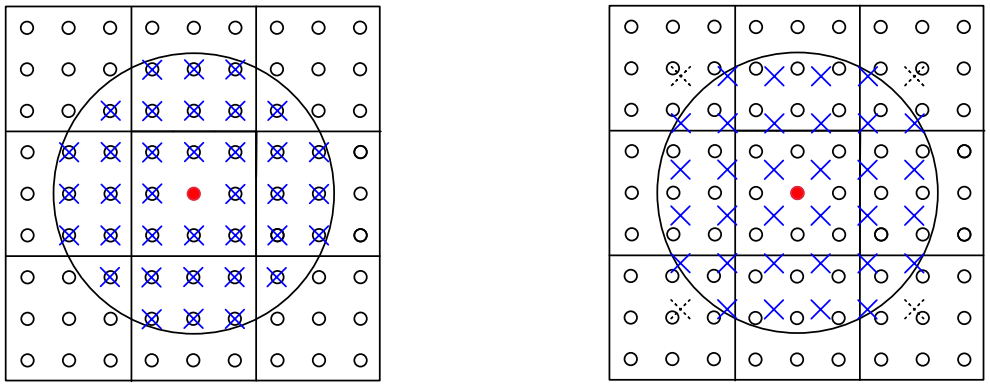

(a) Element-based.

(b) Ball-based.

Figure 4.11: Considered schemes for the placement of quadrature points in 2D. Outer quadrature points are indicated by circles; inner quadrature points for the red point are represented by blue crosses.

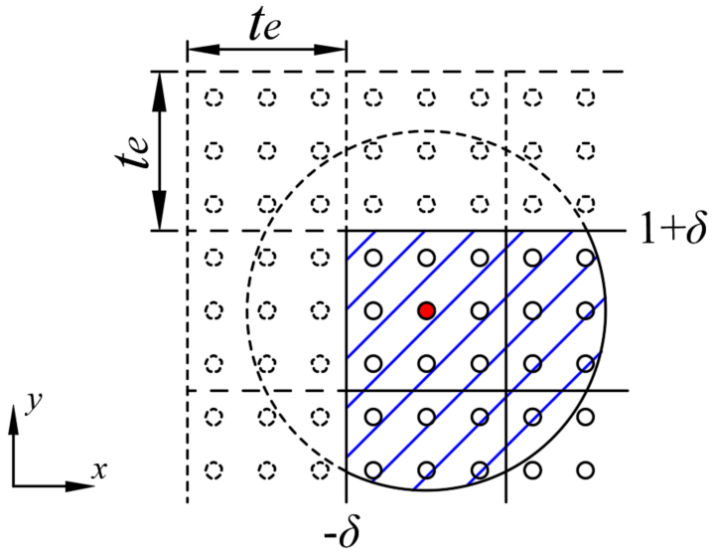

Figure 4.12: The reduced inner integration domain of the red point (blue shadow region) and a mesh extension with size t_e.

4.3.3 Numerical results for uniform discretizations

In this subsection, the convergence behaviour of GMLS-based quadrature on 2D uniform discretizations is investigated. For the δ-convergence study, m is chosen as 2 and 3. Both $\omega_{2,r}$ and $\omega_{2,c}$ are considered in the numerical tests. For simplicity, the mesh is built uniformly over $[-\delta, 1+\delta] \times [-\delta, 1+\delta]$ with spacing h. Then N_q outer quadrature points are placed in each element uniformly in the way shown in Fig. 4.11, while $N_q = 16$ is fixed for all the element. For the ball-based method, $\bar{N}_{qp} = 64$. The extension $t_e = \delta$ is considered as discussed in 1D, the mesh domain thus becomes $[-2\delta, 1+2\delta] \times [-2\delta, 1+2\delta]$. Fig. 4.13 and Fig. 4.14 show second-order convergence behaviours which is consistent with the results in 1D. However, the refinement in 2D is limited by the computer performance. Although the sparse matrix is used, the direct solver still leads to memory issues in the solving, while the error in iterative solvers is not negligible for further refinements. Therefore, this thesis only discusses numerical results for $\log_{10} \left\| u^h - u \right\|_2 > -4$.

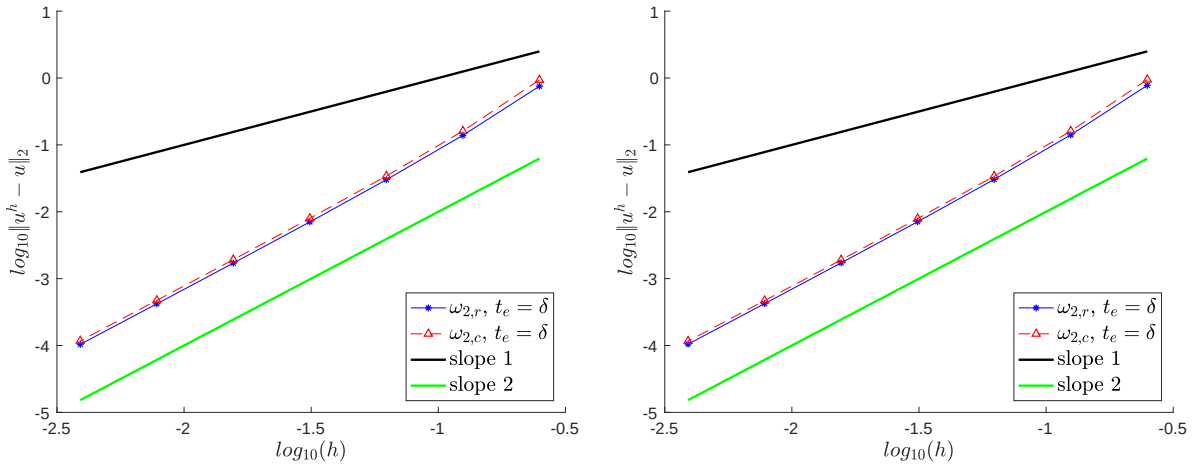

(a) Element-based (b) Ball-based

Figure 4.13: Convergence behaviour for the 2D sinusoidal exact solution. Uniform discretization with $m = 2$.

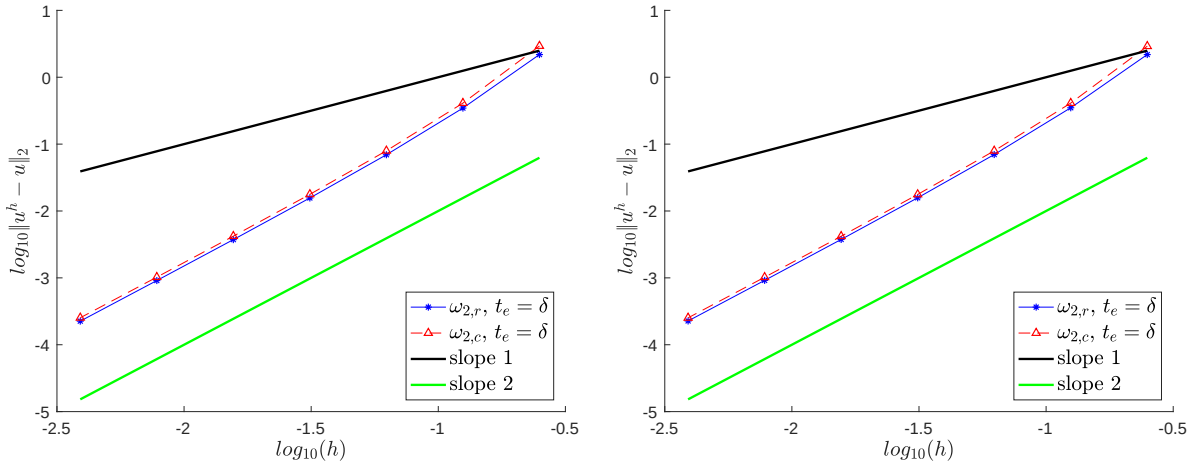

(a) Element-based (b) Ball-based

Figure 4.14: Convergence behaviour for the 2D sinusoidal exact solution. Uniform discretization with $m = 3$.

4.3.4 Numerical results for non-uniform discretizations

As introduced in the previous subsection, the 2D mesh is defined using the concept of tensor product, i.e. $\Omega^2 = \Omega_x^1 \times \Omega_y^1$, where the superscript represents the dimension. For the 2D non-uniform discretization, the perturbation is added to both Ω_x^1 and Ω_y^1 in the way introduced in Subsection 4.2.4, while the edges of Ω are still fixed. This results in a non-uniform mesh with rectangle elements, as shown in Fig. 4.15. Then $N_q = 16$ quadrature points are placed uniformly in each element. In this case, the element-based method still can't converge. The performance of ball-based method with $\bar{N}_{qp} = 64$ is shown in Fig. 4.16. In the range of available results, the convergence rate is 2 and no plateau behaviour is observed.

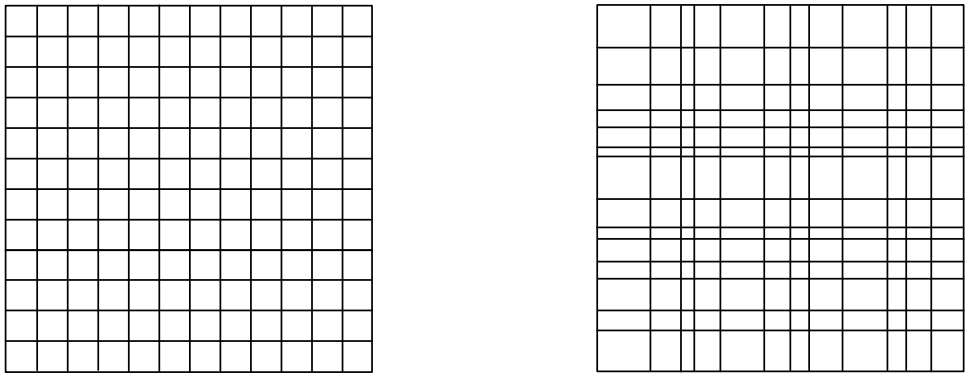

(a) Uniform.

(b) Non-uniform.

Figure 4.15: Examples of uniform and non-uniform discretizations in the 2D domain.

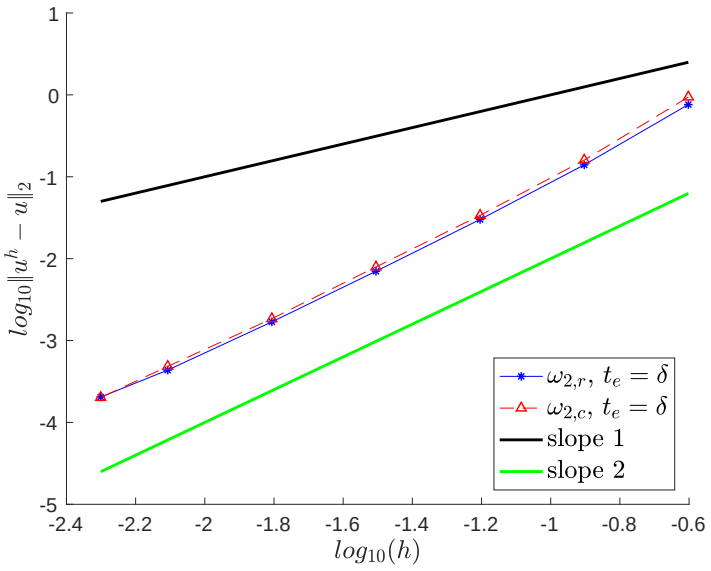

Figure 4.16: Convergence behaviours for the 2D sinusoidal exact solution using ball-based method. Non-uniform discretization with $\epsilon = 0.1$ and $m = 2$.

In the 2D numerical test, an open source optimized compiler for Python, Numba, is used to improve computational efficiency. However, a high refinement will still raise memory and precision issues. The code optimization is thus a potential future work. A thorough comparison between the GMLS-based method and other established method, e.g. Gaussian quadrature, is also needed for further study.

Chapter 5

Nonlocal interactions in nanoscale strain engineering

This chapter studies nonlocal interactions in the nanoscale strain engineering, which are dominated by the LJ potential. The atomistic system consists a monolayer MoS_2 and a multihole Si_3N_4 substrate and the system is simulated by continuum mechanics. A simplified low-dimensional model is investigated before introducing the realistic model. This chapter includes necessary atomic force microscopy (AFM) data and molecular dynamics (MD) results courtesy of Moon-ki Choi and Prof. Ellad Tadmor, University of Minnesota. The open source code LAMMPS is used for MD simulations.

5.1 Nonlocal interactions in the low-dimensional model

For a more realistic 2D shell model, the interaction of 1D beam with a 1D gapped substrate is investigated in this section. There's no real material parameter involved since the low-dimensional model is the proof of concept, units are thus omitted in this section. Leveraging tIGAr introduced in Section 2.2, the beam in this section is divided into 2000 elements using B-spline with polynomials of degree 2.

5.1.1 1D beam with exact 1D substrate interactions

An Euler-Bernoulli beam of length $L = 1000$ is considered with periodic BCs at two ends to simulate a 1D uniform chain of atoms with density $\rho_b = 1$ (number of atoms per unit length). For simplicity, the beam element only has 1 degree of freedom in the z direction (vertical direction). The elastic energy of the beam is given as:

$$U_e = \int_0^L \frac{1}{2} EI \left(\frac{\partial w^2}{\partial x_b^2} \right)^2 dx_b, \tag{5.1}$$

where $EI = 1000$ is the flexural rigidity of the beam, $w(x_b)$ is the deflection of the beam at x_b in the z direction. The beam interacts with a 1D 50% gapped substrate as shown in Fig. 5.1 , while each side of the substrate has size $L_s = 250$ and fixed position $z_s = 0$. Similar to the beam, the substrate also simulates a 1D uniform chain of atoms with uniform density $\rho_s = 1$. The interaction is governed by the LJ potential introduced in Section 1.3. The LJ potential density of the beam at position x_b is computed by integrating the contribution from the all the atoms on the substrate. By considering the periodic BCs, the LJ energy

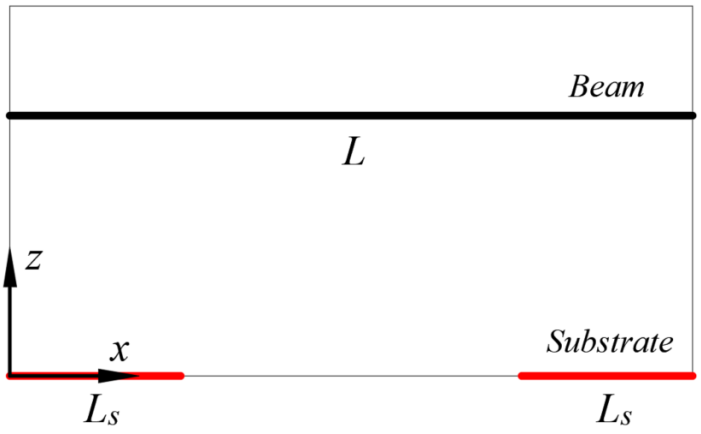

Figure 5.1: 1D beam and 1D gapped substrate system

density at x_b is computed as:

$$U^0_{LJ}(x_b, z_b) = \rho_b \int_{-L_s}^{L_s} \rho_s \phi(r(x_s, x_b, z_b))dx_s + \rho_b \int_{L-L_s}^{L+L_s} \rho_s \phi(r(x_s, x_b, z_b))dx_s, \tag{5.2}$$

where $z_b(x_b)$ is the height of the beam at position x_b, $r(x_s, x_b, z_b) = ((x_s - x_b)^2 + z_b^2)^{1/2}$ and $\phi(r)$ is defined by Eq. (1.6) with $\sigma = \epsilon = 1$. Then the LJ potential of the beam is given as:

$$U_{LJ} = \int_0^L U^0_{LJ}(x_b, z_b)dx_b, \tag{5.3}$$

The total energy of the system is the sum of U_e and U_{LJ}:

$$\Pi = U_e + U_{LJ}. \tag{5.4}$$

Based on the variational principle, the equilibrium configuration of the beam can be obtained by solving the following equation using Newton's iteration, which minimizes the system energy.

$$\delta\Pi = \delta U_e + \delta U_{LJ} = 0 \tag{5.5}$$

In the context of FEniCS, the unknown variable is set as z_b, and w equals to z_b since the undeformed beam is straight. Based on Eq. (5.4), the deflection of the 1D beam after

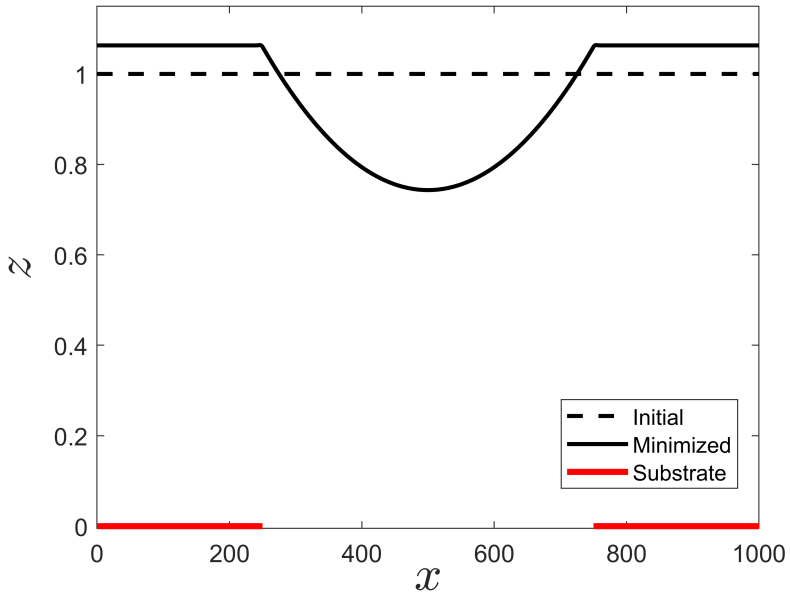

Figure 5.2: Energy minimization of the 1D beam with exact substrate interaction

the minimization as shown in Fig. 5.2 is referred to as the analytical solution of the 1D problem, since the integration of the LJ potential over the substrate is exact. The initial position of the beam is chosen as $z_b^0 = 1$.

5.1.2 1D beam with approximated 1D substrate interactions

However, in higher-dimensional problem, e.g. 3D substrate with holes, it's complicated to derive analytical integration of the LJ potential over the substrate. The numerical integration is thus considered to approximate the integration. As shown in Fig. 1.1, the minimum of the LJ potential is within the short range of r, while the LJ force is also relatively significant in the short range. The LJ force of two particles in the radial direction

is computed as $f_{LJ,r} = -\partial\phi/\partial r$, and the force is $f_{LJ,z} = -\partial\phi/\partial z$ in the z direction. To reduce the number of quadrature points, which dominates the computation cost, it's reasonable to ignore the LJ force from long range effect so that the integration domain can be reduced. With the given 1D non-physical parameters, the minimum $r_m \approx 1.12$. Change of $f_{LJ,r}$ near r_m is shown in Fig. 5.3, which indicates $f_{LJ,r}(r_m) = 0$. Based on the

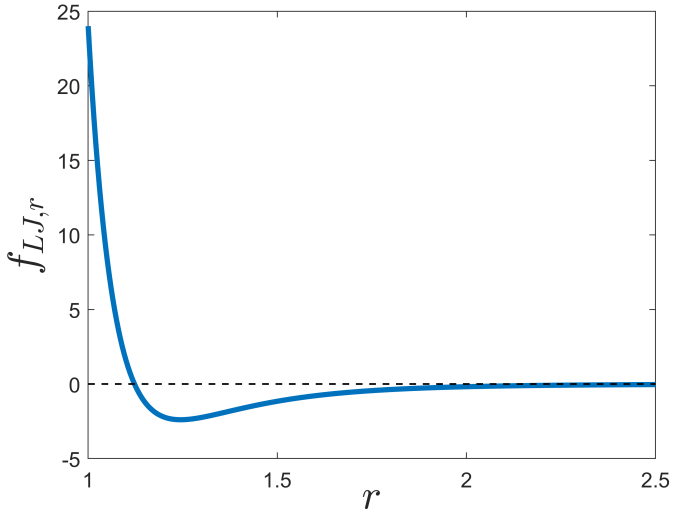

Figure 5.3: Change of $f_{LJ,r}$ near the minimum of ϕ

value of $f_{LJ,r}$, the effective LJ distance for the 1D problem is chosen as $r < r_e \approx 10$, where the force has the magnitude 10^{-6}. Considering the minimization of the beam ($z_b \approx 1$), the integration domain over the substrate for a beam point x_b is defined as $[x_b - \mu, x_b + \mu]$, where $\mu = 10$.

There are three types of quadrature introduced in Chapter 3, while they may not all suitable for this type of problem. Considering the complex geometry in higher-dimensional substrate, the construction of quadrature based on Gaussian quadrature or GMLS will be costly if one wants to maintain high accuracy. Although the Riemann sum method

may be relatively inaccurate for a given number of quadrature points, it is cheaper to be constructed and flexible enough for different geometries. For these reasons, the Riemann sum is chosen as the quadrature scheme for this chapter. As shown in Fig. 5.4, the

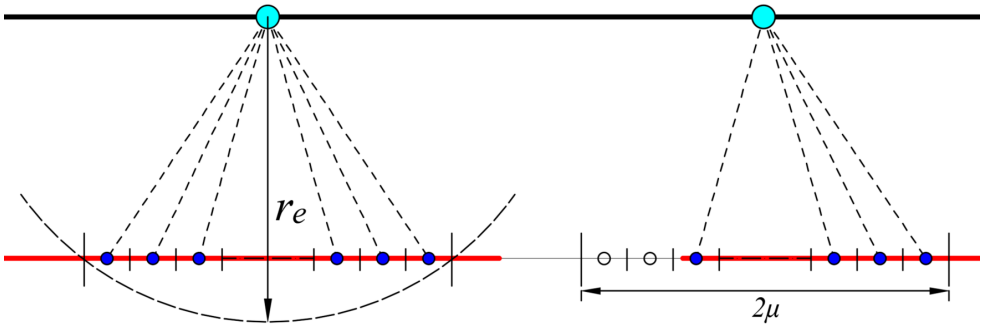

Figure 5.4: Discretizations for the quadrature over the 1D substrate, points on the beam is cyan and valid quadrature points on the substrate is blue. In the full volume method for the approximation of the hole's effect, the contribution from white points are fully ignored.

the reduced domain over the substrate is discretized by a finite number of spacings with quadrature points x_s^q placed on the center of each spacing. If the quadrature point fall on the range of the gap, i.e. $x_s^q \in [L_s, L - L_s]$, the contribution of it will be ignored, as shown in RHS of Fig. 5.4. The numerical integration of LJ energy density is stated as:

$$U_{LJ}^0(x_b, z_b) \approx \rho_b \rho_s \sum_{q=1}^{N_R} \phi(r(x_s^q, x_b, z_b)) w_s^q \tag{5.6}$$

where N_R is the number of spacings, and w_s^q is the quadrature weight which equals to the length of the spacing Δx_s^q. Considering the gap, w_s^q is set to be 0 if $x_s^q \in [L_s, L - L_s]$, which is referred to as the full volume method. The discretization is uniform so that each valid quadrature point, i.e. $x_s^q \notin [L_s, L - L_s]$, has the same weight. To study the performance of the Riemann sum with different discretizations, the force density for the

beam in the z direction ($F^0_{LJ,z} = -\partial U^0_{LJ}/\partial z$) with the non-gapped substrate ($L_s = 500$) is computed using Eq. (5.6) with $N_R = 16,\ 32,\ 64$ at different z_b. Fig. 5.5 shows that

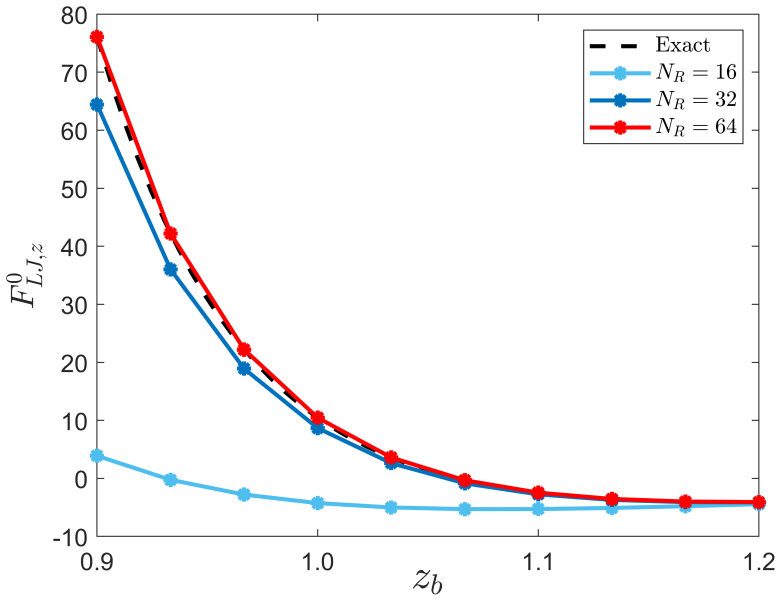

Figure 5.5: Comparison of $F^0_{LJ,z}$ with different discretizations (for the 1D non-gapped substrate)

a higher refinement leads to a better integration. When the gapped substrate is consider, the discretization effect is consistent with the previous study as shown in Fig. 5.6 . Small discrepancy remains over the gapped region. In the full volume method, the quadrature weight is fully considered when the gap effect is approximated, i.e. spacings (weights) fall on edges of the gap are either over or less estimated. As a result, small discrepancy remains near edges of the gap, and the error is enlarged when x_b closes to $L/2$, while there's no force applies on $x_b \in [250 + \mu, 750 - \mu]$ in the approximation. This error can be reduced by further refinement.

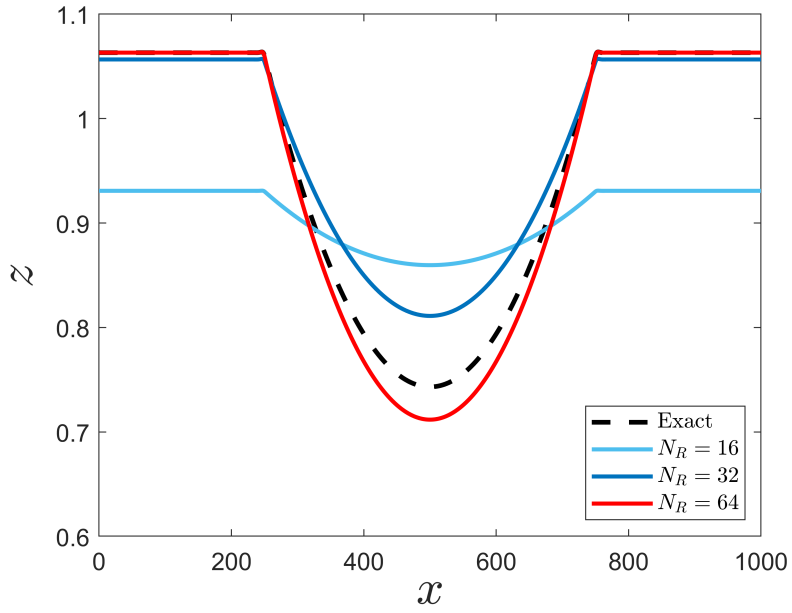

Figure 5.6: Comparison of the minimization with different discretizations in the 1D problem

5.2 Nonlocal interactions in the higher-dimensional model

The realistic problem involves a 3D multihole Si_3N_4 substrate and a 2D monolayer MoS_2. The substrate is shown in Fig 5.7, where D_h is the diameter of each hole and the distance between closest holes is $2D_h$ which is identical over the hole substrate. Considering the given geometry and for simplicity, the system is sliced to diamonds uniformly by the dash line and only one diamond piece of the monolayer (yellow region) is simulated. The diamond has length of $L = 2D_h = 400$ nm, while periodic BC is applied to all sides of it. In the following sections, the left lower corner of the diamond is always set as $[0, 0]$ for reference. NURBS with polynomials of degree 2 is used for discretizations of the shell.

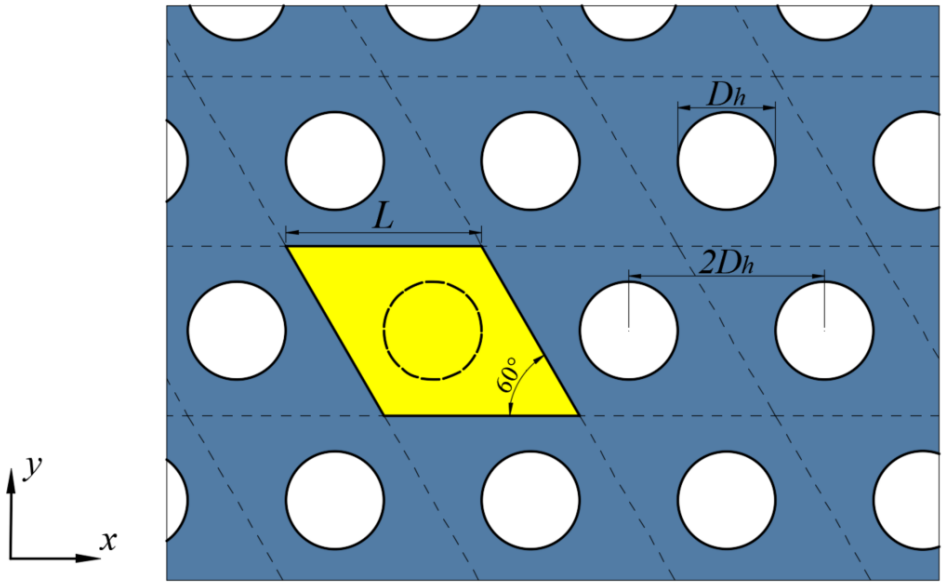

Figure 5.7: Geometry of the 3D multihole substrate and the sliced 2D layer (in yellow)

5.2.1 Structural mechanics of the continuum shell model

The continuum shell in this chapter is modeled follow the Kirchhoff–Love (KL) theory [35, 36]. The theory assumes the cross sections normal to the middle surface remain straight and normal to the middle surface in the deformed configuration, which implies that transverse shear strains are neglected. It further assumes the thickness does not change during the deformation. Based on the reasonable assumptions for thin structures, the theory reduces the dimension of the problem, i.e. completely defines the shell from its middle surface. The elastic part of internal virtual work in Eq. (5.5) is formulated as:

$$\delta U_e = \int_\Omega \mathbf{S} : \delta\mathbf{E} \, d\Omega, \tag{5.7}$$

where $\mathbf{E}$ is the Green-Lagrange strain tensor and $\mathbf{S}$ is the second Piola–Kirchhoff stress tensor which depends on $\mathbf{E}$. The kinematics of the KL shell model as well as the precise

dependence of E on displacement are introduced in [35, 36] in details. The KL theory has no special limitations on the constitutive modeling. In this thesis, the shell is modeled as hyperlastic, which derives $\mathbf{S}$ from the strain energy density Ψ [37]:

$$\mathbf{S} = \frac{\partial \Psi}{\partial \mathbf{E}}. \tag{5.8}$$

This thesis uses the St. Venant–Kirchhoff (SVK) material model which simply extends the simple linear elastic model to the geometrically nonlinear regime. Ψ in the SVK model is assumed as:

$$\Psi = \frac{1}{2}\mathbf{E} : \mathbf{C} : \mathbf{E}, \tag{5.9}$$

where $\mathbf{C}$ is a fourth-rank elasticity tensor depends on the Young's modulus E and Poisson's ratio ν. Then a linear relation between $\mathbf{S}$ and $\mathbf{E}$ can be obtained:

$$\mathbf{S} = \mathbf{C} : \mathbf{E} \tag{5.10}$$

For the KL shell analysis in the context of tIGAr, this thesis uses an open-source library developed by David Kamensky in 2020, called ShNAPr [38], which is developed for Shell Nonlinear Analysis Programs using tIGAr.

5.2.2 Derivation of Elastic constants and thickness for continuum model

To simulate the deformation of the monolayer MoS_2 using continuum shell model, the thickness t and elastic constants, i.e. Young's Modulus E and Passion's ratio ν, are needed. While there are several studies [39, 40] that have investigated elastic properties of

the monolayer MoS_2, the continuum shell model is established for the specific interaction problem and aimed to efficiently approximate results of MD, so the effective constants are estimated in this subsection based on classical elastic problems. A uniaxial tensile test and a bending test for a monolayer MoS_2 are built using MD, which is enough for the derivation of the desired constants (E, ν and t). The Possion's ratio can be directly obtained from the tensile test as shown in Fig. 5.8. Positive strains ε_{xx} are applied in the

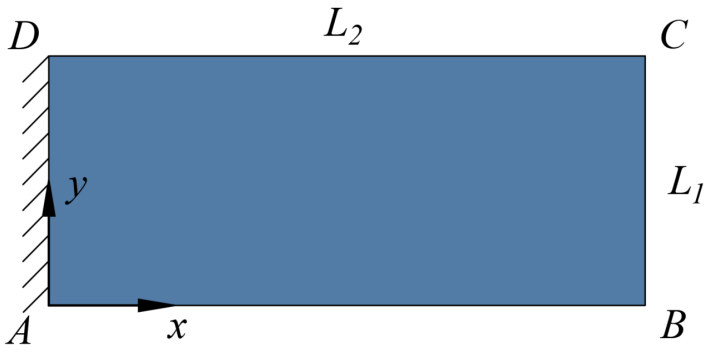

Figure 5.8: The monolayer MoS_2 for the uniaxial tensile test

x direction while AD is fixed and the periodic boundary condition (PBC) is applied to both AB and CD, which implies $\varepsilon_{yy} = 0$. Force on BC, AB and CD can be measured in MD. The generalized Hooke's law with the plane-stress assumption is stated as:

$$\begin{bmatrix} \sigma_{xx} \\ \sigma_{yy} \\ \sigma_{xy} \end{bmatrix} = \frac{E}{1-\nu^2} \begin{bmatrix} 1 & \nu & 0 \\ \nu & 1 & 0 \\ 0 & 0 & 1-\nu \end{bmatrix} \begin{bmatrix} \varepsilon_{xx} \\ \varepsilon_{yy} \\ \varepsilon_{xy} \end{bmatrix}, \tag{5.11}$$

There is no shear component involved in this test. By applying $\varepsilon_{yy} = 0$ to the equation and considering the measured force on each side, the Eq. (5.11) can be reformulate as:

$$\sigma_{xx} = \frac{E}{1-\nu^2}\varepsilon_{xx} = \frac{F_x}{L_1 t}, \tag{5.12}$$

$$\sigma_{yy} = \frac{E\nu}{1-\nu^2}\varepsilon_{xx} = \frac{F_y}{L_2 t}, \tag{5.13}$$

where L_1 and L_2 are dimensions of the monolayer, F_x and F_y are forces applied on AB and CD, respectively. By solving Eq. (5.12) and (5.13), ν can be obtained as:

$$\nu = \frac{\sigma_{yy}}{\sigma_{xx}} = \frac{F_y L_2}{F_x L_1}. \tag{5.14}$$

The tensile test is implemented for both zigzag and armchair direction of MoS_2. The obtained results are close enough for assuming the monolayer MoS_2 is isotropic in plane, while its bending behavior is also isoptoric [39]. The bending test is then built to further determine E and t. Considering the potential deformed shape of the monolayer in the given interaction problem, a uniformly distributed load q (N/m^2 or Pa) is applied on the layer surface in the z direction, while AD and BC are clamped and PBC is still applied on AB and CD. The cross section along the x direction is shown in Fig. 5.9. The reference

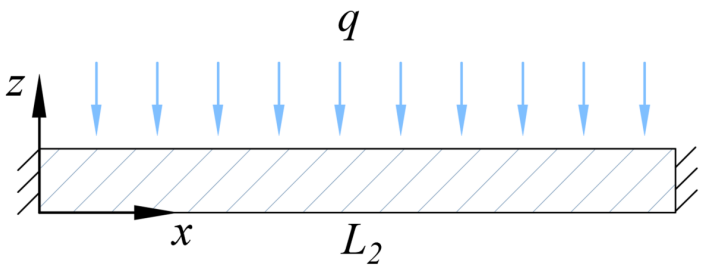

Figure 5.9: The cross section of the monolayer MoS_2 for the bending test

solution of the maximum deflection w_{max} is given by converting the original plane-stress assumption in the Euler–Bernoulli beam theory to the plane-strain assumption, as shown below:

$$w_{max} = \frac{L_2^4 L_1 q}{384 E^* I}, \tag{5.15}$$

where $E^* = E/(1-\nu^2)$, $I = t^3 L_1/12$. By solving Eq. (5.15) together with Eq. (5.12) or (5.13), E and t can be determined for a given set of data. For the tensile test

($L_1 = 1.90051$ nm, $L_2 = 3.29179$ nm), F_x and F_y are measured when $\varepsilon_{xx} = 0.02$, which gives $\nu = 0.2818$ based on Eq. (5.14). For the bending test ($L_1 = 10.1364$ nm, $L_2 = 15.8076$ nm), though the given formula of w_{max} is linear in q for small deformation, the realistic problem may involve significant geometric nonlinearity. As shown in Fig. 5.10, nonlinearity appears in MD simulation as increasing the distributed load q, and three linear fittings (1,2,3) are created to determine three sets of constants ($E = 113.3,\ 95.8,\ 81.0$ GPa, $t = 0.622,\ 0.736,\ 0.870$ nm, respectively). In continuum mechanics, the resistance of a

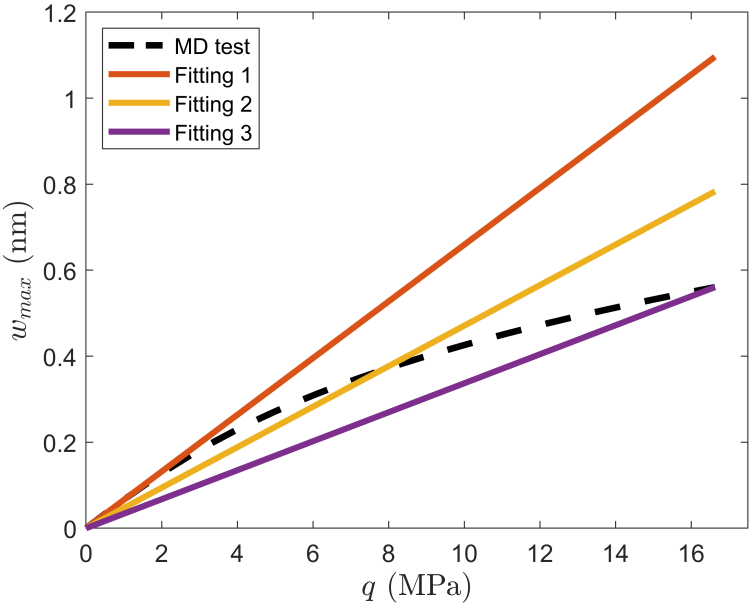

Figure 5.10: Maximum deflection of the bending tests in MD and three linear fittings

shell against bending (bending stiffness) is described as flexural rigidity:

$$D = \frac{Et^3}{12(1-\nu^2)}. \tag{5.16}$$

The flexural rigidity is then calculated as $D = 15.39,\ 21.54,\ 30.11$ eV for fitting 1,2,3, respectively. The bending test is then implemented using the continuum shell model with

the three sets of constants. The results are shown in Fig. 5.10, which shows that larger D allows less deformation. Fitting 1 is chosen as the best fitting and implemented in the following sections. The chosen $D = 15.39$ eV is close to the flexural rigidity investigated in [39], i.e. $8.8 - 13.4$ eV, so the set of constants is considered as a reasonable estimate.

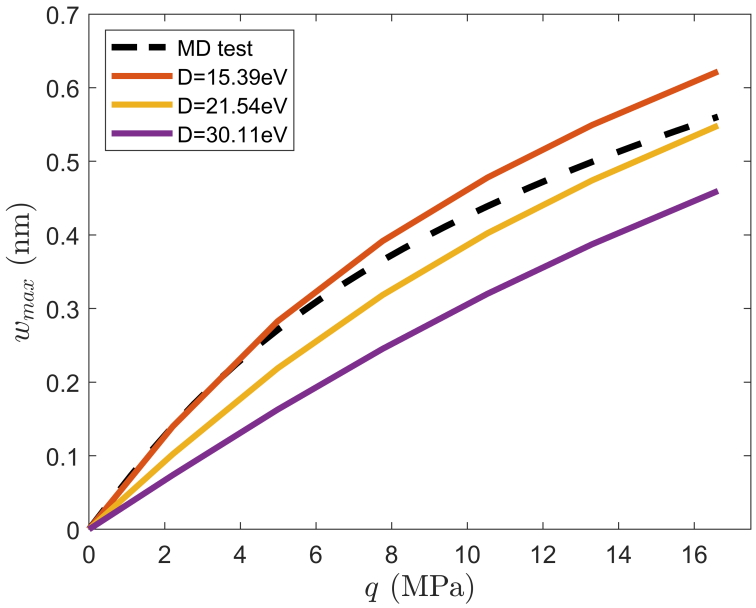

Figure 5.11: Maximum deflection of the bending tests using continuum model with different D

5.2.3 2D shell with 3D multihole substrate

The shell model approximates the monolayer MoS_2 as a continuum and considers a uniform distribution of atoms. The monolayer MoS_2 consists 2 layers of S atoms and a layer of Mo atoms in between, while the atom density of each atom layer is $\rho_{\text{Mo}} = \rho_{\text{S}} = 11.35$ (atoms/nm^2). The distance between a Mo atom and its upper or lower S atom $d_{\text{Mo-S}}$ is

equal to 0.1595 nm. For simplicity, the LJ energy density on S is added to Mo based on the relative position of Mo and S atoms which is assumed as fixed for a MoS_2 molecule during the deformation.

As in 1D, the Si_3N_4 atomistic substrate is approximated as a continuum, while atoms are assumed to be uniform distributed with densities $\rho_{\mathrm{Si}} = 41.8552$ and $\rho_{\mathrm{N}} = 55.8070$ (atoms/nm^3). For a flat substrate with no cylindrical hole, the energy density of a point on the shell can be calculated by analytically integrating the pairwise LJ potential over the semi-infinite substrate and then summing contributions from different types of atom pair $\mathrm{A}-\mathrm{B}$ ($\mathrm{Mo}-\mathrm{Si}$, $\mathrm{Mo}-\mathrm{N}$, $\mathrm{S}-\mathrm{Si}$, $\mathrm{S}-\mathrm{N}$). The integration results in a continuum potential function that only depends on the distance between the shell point and substrate's surface. As the surface is set at 0, the distance is represented by the height of the shell point z_{sh}. The integration is given as:

$$\hat{U}^0_{\mathrm{A-B}}(z_{sh}) = \rho_{\mathrm{A}} \int_{-\infty}^{0}\int_{-\infty}^{\infty}\int_{-\infty}^{\infty} \rho_{\mathrm{B}}\phi_{\mathrm{A-B}}(r)dxdydz = -\gamma\left[\frac{5}{3}\left(\frac{\sigma_{\mathrm{A-B}}}{z_{sh}}\right)^3 - \frac{2}{9}\left(\frac{\sigma_{\mathrm{A-B}}}{z_{sh}}\right)^9\right], \tag{5.17}$$

where $r = (x^2 + y^2 + (z_{sh} - z)^2)^{1/2}$, ρ_{A} is the density of Mo or S in a layer of atoms (atom/nm^2), ρ_{B} is the density of Si or N over the substrate, $\gamma = \frac{2}{5}\pi\rho_{\mathrm{A}}\rho_{\mathrm{B}}\epsilon_{\mathrm{A-B}}\sigma^3_{\mathrm{A-B}}$, $\epsilon_{\mathrm{A-B}}$ and $\sigma_{\mathrm{A-B}}$ are different for different types of atom pair and presented in Table 5.1. LJ parameters for same atoms can be obtained from the interface forcefield and [41, 42]. For different atoms, parameters are derived using the geometric and arithmetic mean.

	ϵ (eV)	σ (nm)
Mo − Si	0.0381	0.3302
Mo − N	0.0778	0.3026
S − Si	0.0017	0.3710
S − N	0.0036	0.3430

Table 5.1: LJ parameters for different atoms

The complete LJ energy density of a shell point $\mathbf{x}_{sh}$ with height z_{sh} interacts with a flat substrate is then calculated as:

$$\begin{aligned}\bar{U}^0_{LJ}(\mathbf{x}_{sh}) = \hat{U}^0_{\text{Mo}-\text{Si}}(z_{sh}) + \hat{U}^0_{\text{Mo}-\text{N}}(z_{sh}) \\ + \hat{U}^0_{\text{S}-\text{Si}}(z_{sh} + d_{\text{Mo}-\text{S}}) + \hat{U}^0_{\text{S}-\text{N}}(z_{sh} + d_{\text{Mo}-\text{S}}) \\ + \hat{U}^0_{\text{S}-\text{Si}}(z_{sh} - d_{\text{Mo}-\text{S}}) + \hat{U}^0_{\text{S}-\text{N}}(z_{sh} - d_{\text{Mo}-\text{S}}),\end{aligned} \tag{5.18}$$

whose minimum (5.18) is around $z_{sh} = 0.42$ nm.

When holes are considered on the substrate, it's difficult to derive the analytical solution of the integral. As in 1D problem, the Riemann sum is used to compute the integration numerically over the substrate with holes. Follow Eq. (5.18), the LJ energy density of a shell point $\mathbf{x}_{sh}$ interacts with a multihole substrate is approximated as:

$$U^0_{LJ}(\mathbf{x}_{sh}) \approx \sum_{q=1}^{N_R} \Phi(r_q) w_s^q, \tag{5.19}$$

where

$$\begin{aligned}\Phi(r_q) = \rho_{\text{Mo}} \left[\rho_{\text{Si}}\phi_{\text{Mo}-\text{Si}}(r_q) + \rho_{\text{N}}\phi_{\text{Mo}-\text{N}}(r_q)\right] \\ + \rho_{\text{S}} \left[\rho_{\text{Si}}\phi_{\text{S}-\text{Si}}(r_q^+) + \rho_{\text{N}}\phi_{\text{S}-\text{N}}(r_q^+)\right] + \rho_{\text{S}} \left[\rho_{\text{Si}}\phi_{\text{S}-\text{Si}}(r_q^-) + \rho_{\text{N}}\phi_{\text{S}-\text{N}}(r_q^-)\right],\end{aligned} \tag{5.20}$$

N_R is the number of quadrature points, $r_q = \|\mathbf{x}_{sh} - \mathbf{x}_s^q\|$, $\mathbf{x}_s^q$ is the q-th quadrature points placed on the substrate for $\mathbf{x}_{sh}$ and w_s^q is the associated quadrature weight. For the given

geometry, the effects of neighbouring holes are ignored since $L \gg r_e$. The full volume method is used as shown in Fig. 5.14, i.e. if $\mathbf{x}_s^q$ falls on a hole, then w_s^q is set to 0. The superscript of r_q represents the distance that considers S layers.

$$r_q^{\pm} = \|(\mathbf{x}_{sh} \pm d_{\text{Mo-S}}\hat{\mathbf{n}}_{sh}) - \mathbf{x}_s^q\|\,, \tag{5.21}$$

where $\hat{\mathbf{n}}_{sh}$ is the unit normal vector at $\mathbf{x}_{sh}$. To build the quadrature rule based on Riemann sum, the integration domain needs to be reduced to a finite range first. The reduction is according to the 'point-wise force density' $f_{LJ,r} = -\partial\Phi/\partial r$, as shown in Fig. 5.12. The effective LJ distance is chosen as $r < r_e \approx 5$ nm, where the magnitude of $f_{LJ,r}$

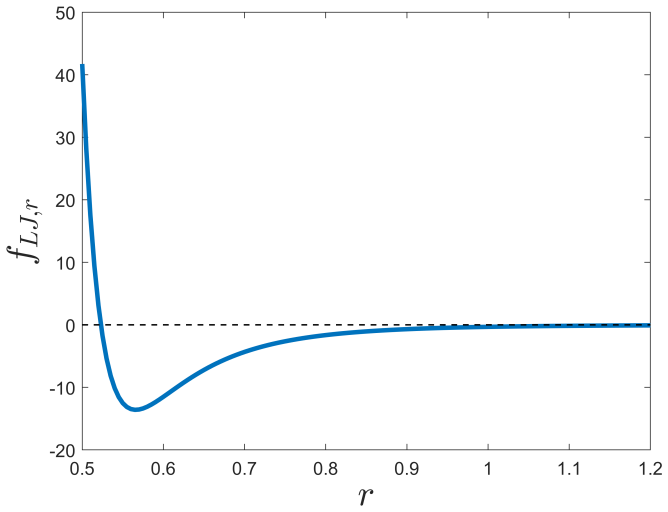

Figure 5.12: Change of $f_{LJ,r}$ near the minimum of Φ

is 10^{-6}. For simplicity, the integration domain for a shell point $\mathbf{x}_{sh}$ is reduced to a cube $[x_{sh}-\mu, x_{sh}+\mu]\times[y_{sh}-\mu, y_{sh}+\mu]\times[0, -\mu]$ with dimension $2\mu\times2\mu\times\mu$ ($L\times W\times H$) so that the volume weight of each quadrature points can be easily computed. According to the effective distance and the minimum, μ is chosen as 5 nm. In 1D, a uniform discretization is used

for quadrature. However, the uniform discretization for a 3D space needs a cube number of quadrature points that used in 1D, which is expensive for the simulation. Considering the concentration of the LJ potential and force, a non-uniform discretization that places points intensively near $\mathbf{x}_{sh}$ can resolve the cost problem. A tree data structure, called octree, is used in the thesis to efficiently build the non-uniform discretization by recursively subdividing the 3D space. While octrees are usually used in 3D graphics and 3D game engines, the criterion of subdivisions is controllable so that the octree can have a desired data structure as user's requirement. To illustrate the method, a quadtree, which is a 2D analog of the octree, is shown in Fig 5.13. together with a 1D beam as an example.

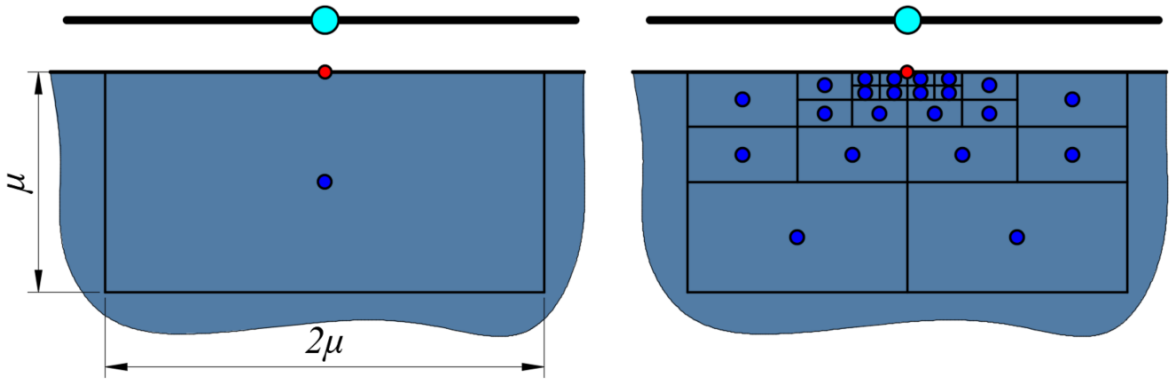

(a) 0-th generation

(b) 4-th generation

Figure 5.13: Evolution of a quadtree, a 2D analog of the octree. The red point is the projection of the cyan beam point, blue points are quadratrue points.

The structure starts from the undivided rectangle, which is defined as the 0-th generation of subdivision. The quadrature point is placed at the centre of the rectangle and the area of the rectangle is the associated quadrature weight. Then in the following

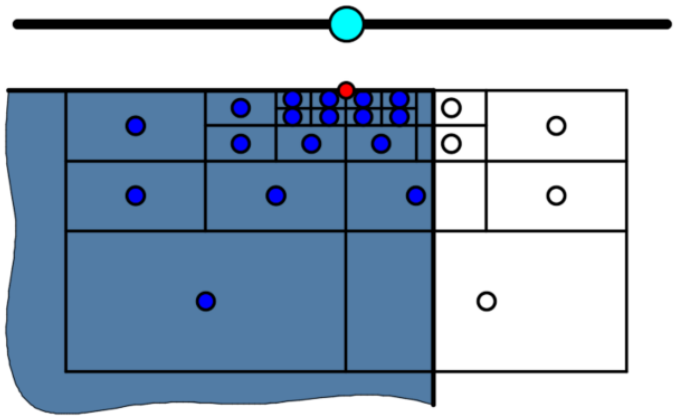

Figure 5.14: The octree quadrature with the full volume method for the approximation of hole's effect. Quadrature points fall on the hole are white and ignored. Only blue points are considered in the quadrature.

generations, the existent rectangle will be subdivided to 4 small rectangles if the certain criterion is satisfied. The criterion used in this thesis is stated as follow: At p-th generation ($p < n_{max}$), a rectangle will be subdivided if

$$\|\mathbf{x}_s^q - \bar{\mathbf{x}}_{sh}\| < \frac{(\mu^2 + \mu^2)^{1/2}}{2^p} \tag{5.22}$$

where $\mathbf{x}_s^q$ is the quadratrue point of the rectangle, $\bar{\mathbf{x}}_b = [x_b, 0]$ is the projection of the beam point $\mathbf{x}_b$ onto $y = 0$ and n_{max} is maximum number of generation which can ends the subdivision process. In octree, the rectangle increases to a cube which will be divided into 8 small cubes in a subdivision. The quadrature point is placed in the geometric center of the cube and the associated weight is defined as the volume of the cube. The criterion for octree is analogous to the 2D version, i.e. at p-th generation ($p < n_{max}$), a cube will be

subdivided if

$$\|\mathbf{x}_s^q - \bar{\mathbf{x}}_{sh}\| < \frac{(\mu^2+\mu^2+\mu^2)^{1/2}}{2^p} \tag{5.23}$$

where $\mathbf{x}_s^q$ is the quadratrue point of the cube and $\bar{\mathbf{x}}_{sh} = [x_{sh}, y_{sh}, 0]$. To study the performance of octrees, the force density for the shell in the z direction $F^0_{LJ,z} = -\partial U^0_{LJ}/\partial z$ is computed without considering the effect of the hole. The reference (exact) force density is thus computed as $\bar{F}^0_{LJ,z} = -\partial \bar{U}^0_{LJ}/\partial z$. For the octree, $n_{max} = 6, 7, 8$ are considered, which only creates 148, 176, 204 quadrature points, respectively. The comparison near the minimum of $\bar{U}^0_{LJ}$ is shown in Fig. 5.15. Further increasing n_{max} for this criterion does not improve the accuracy significantly, the octree with $n_{max} = 8$ is thus chosen as the quadrature rule considering the simulation cost.

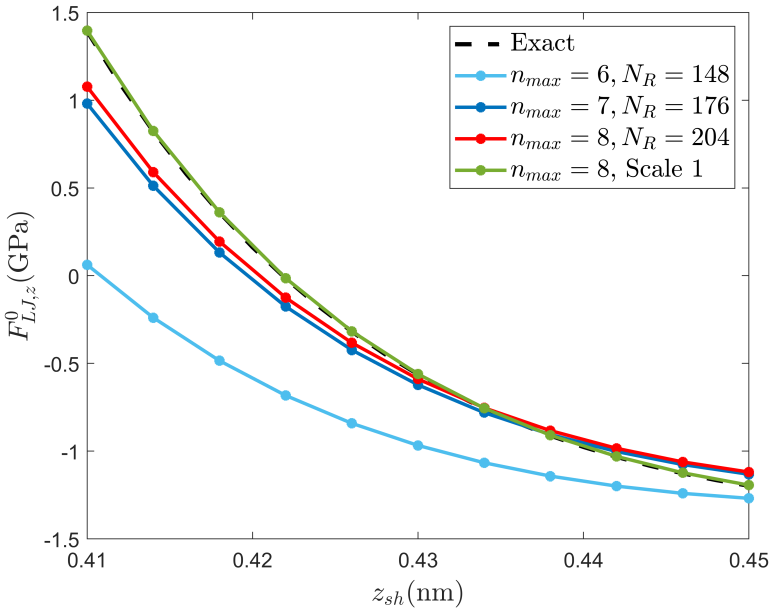

Figure 5.15: Comparison of $F^0_{LJ,z}$ with different octrees including a modified $n_{max} = 8$ (for the 3D flat substrate without holes)

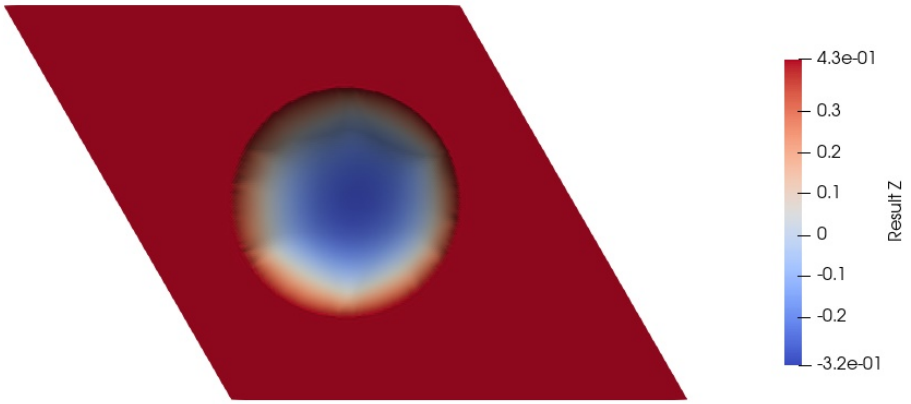

(a) Top view

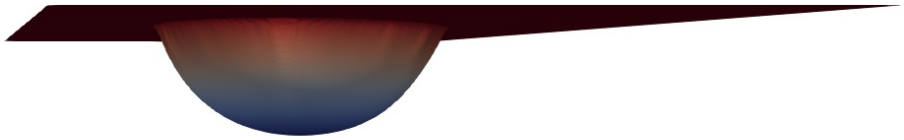

(b) View between front and bottom

Figure 5.16: Energy minimization of the 2D shell in two different views. $L = 400$ nm. The deformation is scaled by a factor 100. The color bar indicates values of z_{sh}

To further improve the accuracy of the chosen quadrature rule, the volume weights are slightly modified. The first step is to match the minimum ($\bar{F}^0_{LJ,z} = 0$). Since the current minimum position of the octree quadrature is lower than the analytical one, the repulsive force contributed by the quadrature points in short range ($r < 0.525$ nm) is amplified. Meanwhile, the attractive contributions from points in long range are reduced to avoid big changes of the repulsive part, which also improves the approximation of the hole's effect using the full volume method. After fitting the minimum, the weights are

scaled again, but simultaneously, to match forces at positions away from the minimum. A possible modification is shown in Fig. 5.15, and the scaling is: $w_r \times 1.05 \times 1.11$ and $w_a \times 0.966 \times 1.11$ (Scale 1), where w_r and w_a are weights for repulsion and attraction, respectively. A simulation result is shown in Fig. 5.16, 200×200 elements are used for the discretization of the shell.

An alternative way to approximate the integration over the substrate follows the concept of 'subtraction' in contrast to the method discussed above. For convenience, the previous method based on Eq. (5.19) is referred to as the plus method (P-method) and the 'subtraction' one is referred to as the minus method (M-method). Using the M-method, the LJ energy density of a shell point $\mathbf{x}_{sh}$ interacts with a multihole substrate is approximated as:

$$U^0_{LJ}(\mathbf{x}_{sh}) \approx \bar{U}^0_{LJ}(\mathbf{x}_{sh}) - \sum_{q=1}^{N_R} \Phi(r_q) w_s^q. \tag{5.24}$$

But in this case, w_s^q is set to 0 if $\mathbf{x}_s^q$ **does not** fall on a hole. This method leads to an accurate approximation for $\mathbf{x}_{sh}$ away from the hole, but it is sensitive to the accuracy of quadrature for the center region where a full subtraction occurs, i.e. all $\mathbf{x}_s^q$ fall on the hole. Another scaling for the quadrature weights is considered: $w_r \times 1.05 \times 1.105$ and $w_a \times 0.966 \times 1.105$ (Scale 2). Even though the two scalings are only slightly different, if the full subtraction happens, the resultant force density shows different signs for a certain range, as shown in Fig. 5.17. This results in a obvious difference of the deflection above the hole as shown in Fig. 5.18. For simplicity, the numerical test use 50×50 elements for a scaled model with $L = 20$nm, which is the smallest scale that the effect

of neighbouring holes can be neglected. While the P-method is not affected by the small difference between Scale 1 and 2, the minimization of the center region using M-method follows the zero-force position shown in Fig. 5.17. Considering the effective distance r_e, the concerned region supposes to feel infinitesimal attractive force from the substrate, but M-method applies additional force, which comes from numerical error, to the region and thus leads to an unstable result. Although M-method is not used for further work, its instability reflects the sensitive nature of the specific nonlocal problem and the weakness of numerical methods, which makes the above study valuable.

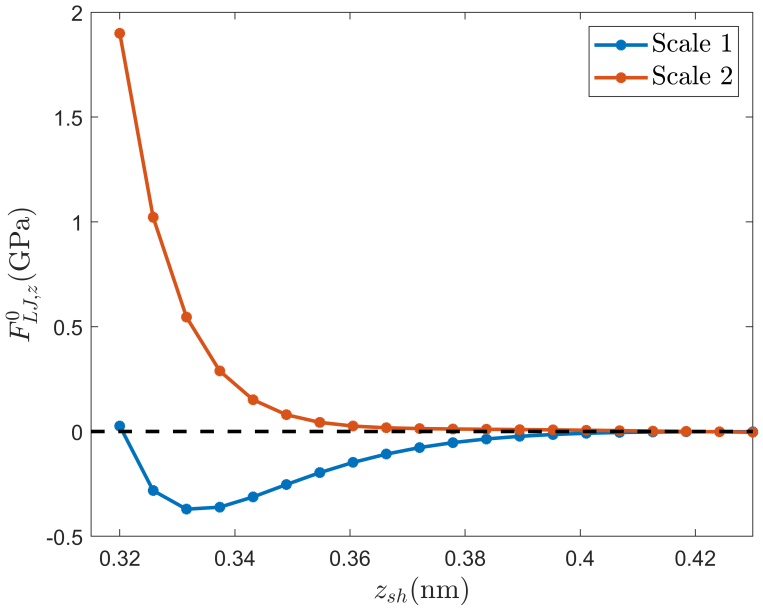

Figure 5.17: Comparison of $F^0_{LJ,z}$ with different scalings for the full subtraction (force density of the center region using M-method)

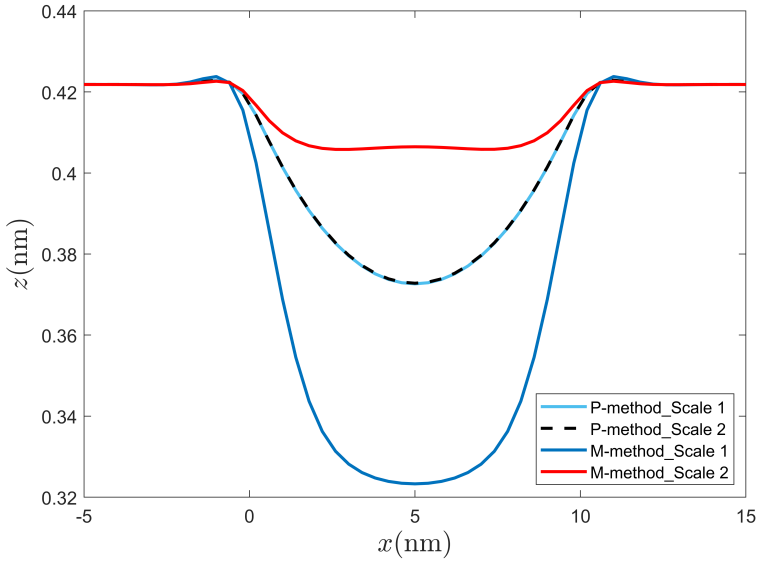

Figure 5.18: The cross section of the shell at $y = 8.66$ nm after minimization with different methods and scalings

5.2.4 2D shell with 3D curved substrate

The multihole substrate is designed to be flat and thus sharp on the hole's edge. However, due to the precision of manufacturing, the surface of the substrate in reality is curved as shown in Fig. 5.19. To simulate the interaction with the curved substrate, the octree needs to be modified again. The highest point of the curved surface is used to determine the datum plane ($z = 0$). Then quadrature points $\mathbf{x}_s^q$ are translated following the shape of the surface:

$$\bar{\mathbf{x}}_s^q = \mathbf{x}_s^q + [0, 0, f_s(x_s^q, y_s^q)] \tag{5.25}$$

where $\bar{\mathbf{x}}_s^q$ are the translated quadrature points and $f_s(x, y)$ is the surface function. If the surface is not analytical, a Taylor approximation of the surface at $\bar{\mathbf{x}}_{sh}$ can be used in the translation since the gradient of the surface can be measured in the context of

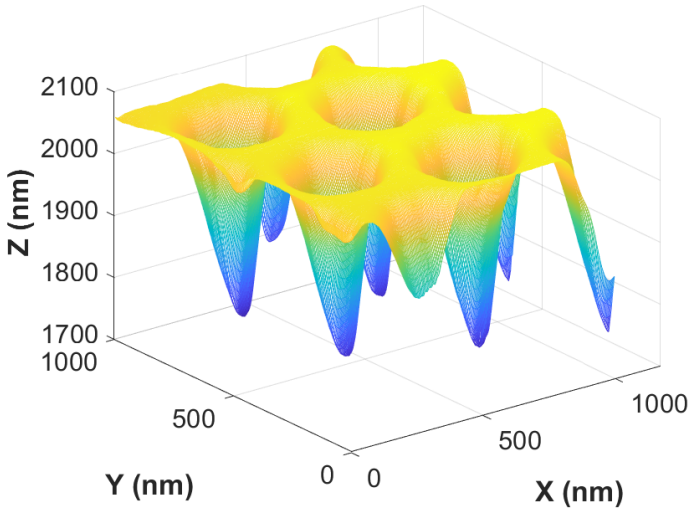

Figure 5.19: AFM result of the substrate from Moon-ki Choi and Prof. Ellad Tadmor, University of Minnesota.

FEniCS. Nevertheless, the curved substrate leads to larger deformations of the shell. In this case, the octree quadrature may encounter with convergence issues. For example, in the solving procedure, a large deformation in an iteration step can cause singularity if the deformed shell partially intersects with the substrate, i.e. some of the r_qs are close or equal to 0. The dynamic relaxation method can resolve this issue by adding damping to the shell, but also results in a large computational cost. An alternative approach to deal with the curved surface is considered. For a surface with small curvature near $\bar{\mathbf{x}}_{sh}$, the integration of the LJ potential over the substrate can be approximated by Eq. (5.18) considering its concentrated nature. Again, a low-dimensional model shown in Fig. 5.20 illustrates the approximation. The tangent plane of the surface at $\bar{\mathbf{x}}_{sh}$ is built to determine d_t which is the distance between $\mathbf{x}_{sh}$ and the plane. Then according to Eq. (5.18), the approximated LJ energy density of $\mathbf{x}_{sh}$ interacts with a curved substrate is calculated

as $\bar{U}^0_{LJ}(d_t)$. This approximation is referred to as the tangent method (T-method). In the

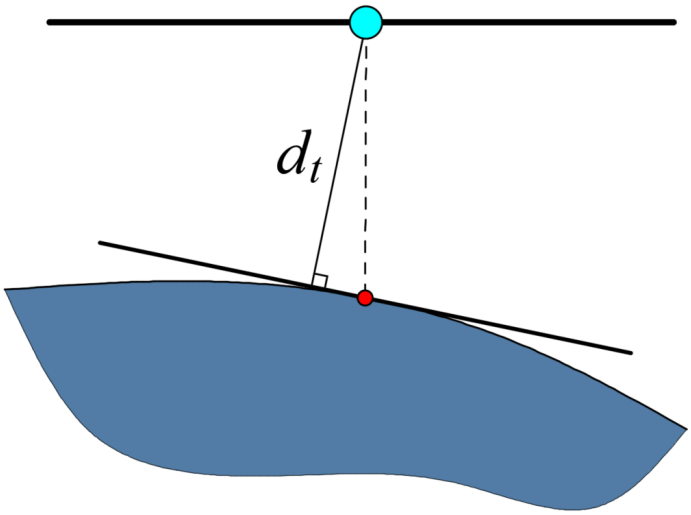

Figure 5.20: A low-dimensional version of the tangent method. The red point is the projection of the cyan point on the substrate.

context of FEniCS, the energy density defined by the tangent method is more concise than the one from octree quadrature, which leads to a much lower computational cost of the assembly procedure at each iteration step of the solving. Therefore, the tangent method is more compatible with dynamic relaxation. A simple analytical substrate is introduced to investigated performances of the tangent method. For simplicity, the scaled model with $L = 20$ nm is used. To be analogous to the real substrate, the surface is defined as a squared cosine function:

$$f_s(r_c(x,y)) = \begin{cases} -A(0.5(\cos\dfrac{\pi r_c}{8}+1))^2 & \text{for } r_c \leq 8, \\ \\ 0 & \text{for } r_c > 8, \end{cases} \tag{5.26}$$

where $r_c(x,y) = \|[x,y] - \mathbf{x}_c\|$, $\mathbf{x}_c = [x_c, y_c]$ is the center of the diamond, and A is the amplitude factor. Fig. 5.21 shows the result for $A = 8$ using different approximation

methods with 50×50 elements. The difference between the two methods is relatively small compared with the overall deflection. Varies of A (range from 1 to 8) have been test and T-method shows a stable behaviour. The T-method is thus chosen for the future study, mainly for interactions with curved geometry.

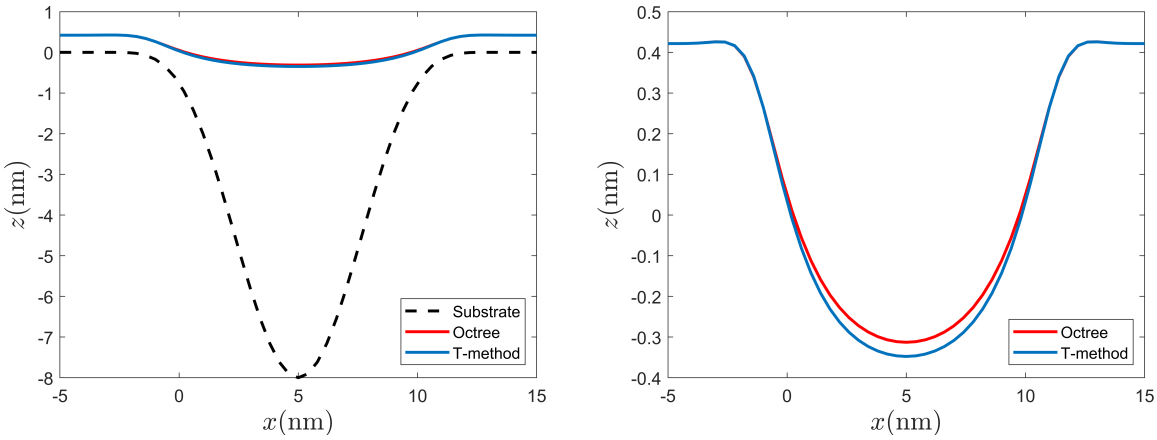

(a) With substrate (b) Zoomed

Figure 5.21: The cross section of the shell at $y = 8.66$ nm after energy minimization. Two approaches are considered to approximate the interaction with the curved substrate whose surface is indicated by the dash line.

Fig. 5.22 shows a result for an approximated real substrate ($L = 400$ nm) using T-method with 100×100 elements. For simplicity, the surface of the curved substrate is approximated by solving a modified Helmholtz equation over the diamond domain:

$$\begin{cases} -\varepsilon^2 \nabla^2 u + (u - H) = 0, & \text{for } r_c \geq 100 \text{ nm} \\ u = 0, & \text{for } r_c < 100 \text{ nm} \end{cases} \tag{5.27}$$

where $\varepsilon = 20$ and $H = 85$ control the curvature and the depth of the substrate, respectively. The solution of u is shown in Fig. 5.23 and surface is given as $f_s = u - \max(u)$. In this

simulation, no force is applied on $r_c < 100$ nm which is the region above the designed hole. When the curved substrate is considered, the region is far enough from the substance and thus its interaction is negligible.

This subsection is also a preliminary study for potential future work. The low computational cost of the T-method allows further studies on multilayer MoS_2. Meanwhile, alternative ways to determine d_t are valuable to be investigated for increasing the accuracy of the approximation and for matching the bend-contour from experiments.

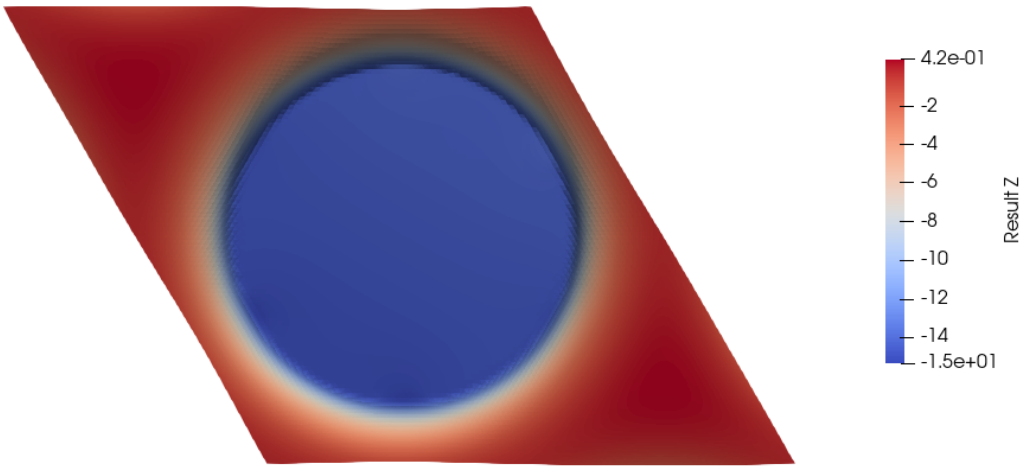

(a) Top view

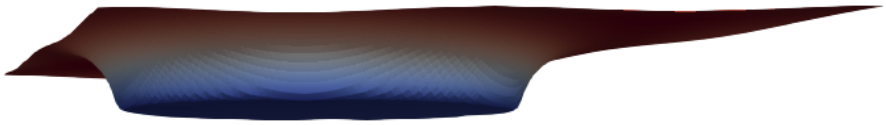

(b) View between front and bottom

Figure 5.22: Energy minimization of the 2D shell interacting with an approximated curved substrate. $L = 400$ nm. The deformation is scaled by a factor 3. The color bar indicates values of z_{sh}

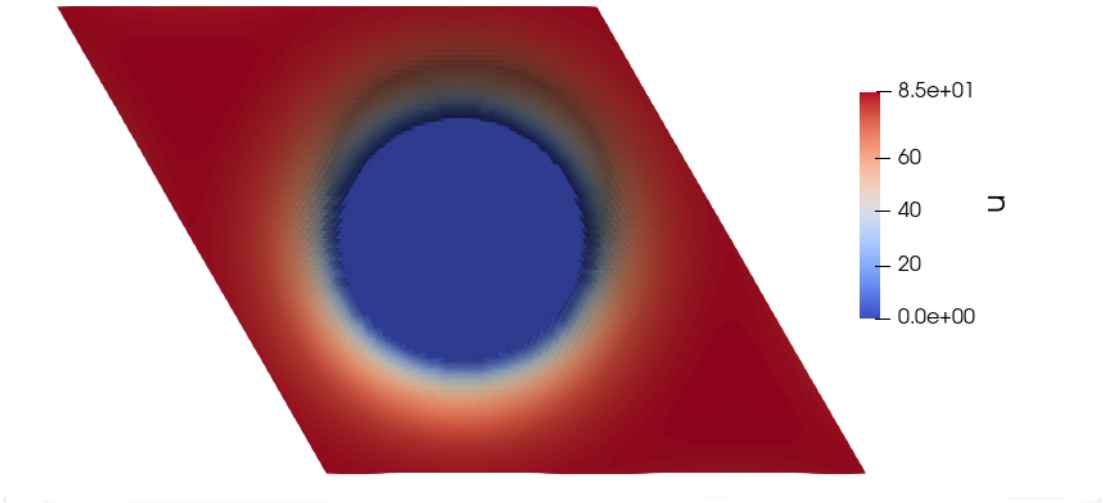

(a) Top view

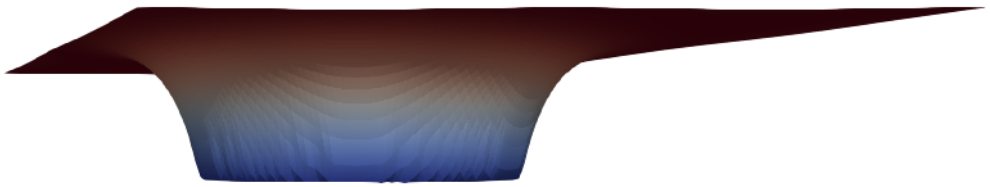

(b) View between front and bottom

Figure 5.23: Solution of Eq. (5.27) over the diamond domain, which represents the substrate surface for the minimization shown in Fig. 5.22

Chapter 6

Conclusion

Nonlocal interactions have shown wide applicability for describing long-range effects from microscale to macroscale. However, nonlocal problems raise numerical challenges such as high computational cost and geometric complexity. For this reason and in the context of continuum mechanics, this thesis studies numerical methods for nonlocal problems and focuses on two topics: weak form peridynamics and nanoscale strain engineering.

For weak form peridynamics, the GMLS-based quadrature rule is used for both inner and outer integration. Two methods, element-based and ball-based, are considered for the placement of inner quadrature points. The mesh is extended for the construction of inner quadrature so that symmetry is maintained. In the numerical tests for 1D uniform discretizations, both element-based and ball-based methods show stable convergence and the mesh extension improve the first-order convergence to the second-order. For 1D non-uniform discretizations, only the ball-based method is capable of retaining symmetry and show convergence. While a plateau behaviour arises during the mesh refinement in the

non-uniform tests, increasing the number of outer quadrature points leads to a more persistent second-order convergence. Within the computational limitation, similar numerical tests have been done in 2D and result in consistent behaviours as shown in 1D tests. In conclusion, the symmetry is an important property for the convergence of GMLS-based method.

For the nanoscale strain engineering, the thesis aims at leveraging continuum models to simulate nonlocal interactions, which are governed by the LJ potential, between a monolayer MoS_2 and a multihole Si_3N_4 substrate. A 1D beam and 1D substrate are first built for preliminary study and the interaction in such low-dimensional model can be formulated analytically. An effective interaction distance is determined considering the concentrated nature of the LJ model. The Riemann sum is chosen as the quadrature rule for integration over the substrate while approximating the effect from holes. When the model upgrades to higher-dimension, a 2D Kirchhoff–Love shell is built to simulate the monolayer. The effective elastic constants and thickness for the shell are determined according to classical elastic tests performed in MD. The Riemann sum for the 3D substrate is optimized using octrees. The chosen structure acheives low computational cost by intensively placing quadrature points in the short-range of LJ force which dominates the nonlocal interaction. For future work, the realistic substrate has shown curvature due to manufacturing precision, so an alternative approach based on a semi-infinite integral is proposed to approximate the integration over the curved substrate, thus avoiding the convergence and cost issues of Riemann sums when dealing with such substrates.

Reference

[1] Priya Johari and Vivek B. Shenoy. Tuning the electronic properties of semiconducting transition metal dichalcogenides by applying mechanical strains. *ACS Nano*, 6(6):5449–5456, 2012. PMID: 22591011.

[2] Lei Yang, Xudong Cui, Jingyu Zhang, Kan Wang, Meng Shen, Shuangshuang Zeng, Shadi Dayeh, Liang Feng, and Bin Xiang. Lattice strain effects on the optical properties of MoS_2 nanosheets. *Scientific reports*, 4:5649, 07 2014.

[3] H. Peelaers and C. G. Van de Walle. Effects of strain on band structure and effective masses in MoS_2. *Phys. Rev. B*, 86:241401, Dec 2012.

[4] Christian Martella, Carlo Mennucci, Eugenio Cinquanta, Alessio Lamperti, Emmanuele Cappelluti, Francesco Buatier de Mongeot, and Alessandro Molle. Anisotropic MoS_2 nanosheets grown on self-organized nanopatterned substrates. *Advanced Materials*, 29(19):1605785, 2017.

[5] S.A. Silling. Reformulation of elasticity theory for discontinuities and long-range forces. *Journal of the Mechanics and Physics of Solids*, 48(1):175 – 209, 2000.

[6] S.A. Silling, M. Epton, O. Weckner, Jifeng Xu, and E. Askari. Peridynamic states and constitutive modeling. *Journal of Elasticity*, 88:151–184, 2007.

[7] S.A. Silling and R.B. Lehoucq. Peridynamic theory of solid mechanics. In Hassan Aref and Erik van der Giessen, editors, *Advances in Applied Mechanics*, volume 44 of *Advances in Applied Mechanics*, pages 73 – 168. Elsevier, 2010.

[8] Erdogan Madenci and Erkan Oterkus. *Peridynamic Theory and Its Applications*. Springer, 2013.

[9] S. Silling, Olaf Weckner, E. Askari, and Florin Bobaru. Crack nucleation in a peridynamic solid. *International Journal of Fracture*, 162:219–227, 03 2010.

[10] Youn Doh Ha and Florin Bobaru. Studies of dynamic crack propagation and crack branching with peridynamics. *International Journal of Fracture*, 162:229–244, 03 2010.

[11] Bahattin Kilic and Erdogan Madenci. Prediction of crack paths in a quenched glass plate by using peridynamic theory. *International Journal of Fracture*, 156:165–177, 04 2009.

[12] Cagan Diyaroglu, Erkan Oterkus, Erdogan Madenci, Timon Rabczuk, and Amir Siddiq. Peridynamic modeling of composite laminates under explosive loading. *Composite Structures*, 144:14–23, 06 2016.

[13] Dan Huang, Qing Zhang, and Pizhong Qiao. Damage and progressive failure of concrete structures using non-local peridynamic modeling. *Science China Technological Sciences*, 54:591–596, 03 2011.

[14] Ning Zhu, Dennj De Meo, and Erkan Oterkus. Modelling of granular fracture in polycrystalline materials using ordinary state-based peridynamics. *Materials*, 9:977, 12 2016.

[15] Y. Mauricio Muñoz-Muñoz, Gabriela Guevara-Carrion, Mario Llano-Restrepo, and Jadran Vrabec. Lennard-Jones force field parameters for cyclic alkanes from cyclopropane to cyclohexane. *Fluid Phase Equilibria*, 404:150 – 160, 2015.

[16] Hendrik Heinz, R. A. Vaia, B. L. Farmer, and R. R. Naik. Accurate simulation of surfaces and interfaces of face-centered cubic metals using 12-6 and 9-6 Lennard-Jones potentials. *The Journal of Physical Chemistry C*, 112(44):17281–17290, 2008.

[17] Max Born. Eine thermochemische anwendung der gittertheorie. *Verhandlungen der Deutschen Physikalischen Gesellschaft*, 21:13–24, 1919.

[18] J. E. Lennard-Jones. On the determination of molecular fields. *Proc. R. Soc. Lond. A*, 106:463–477, 1924.

[19] Thomas Hughes. *The Finite Element Method: Linear Static and Dynamic Finite Element Analysis*, volume 78. 01 2000.

[20] T.J.R. Hughes, J.A. Cottrell, and Y. Bazilevs. Isogeometric analysis: CAD, finite elements, NURBS, exact geometry and mesh refinement. *Computer Methods in Applied Mechanics and Engineering*, 194(39):4135 – 4195, 2005.

[21] J. Cottrell, Thomas Hughes, and Yuri Bazilevs. *Isogeometric Analysis: Toward integration of CAD and FEA*. Wiley, 2009.

[22] Anders Logg, Garth Wells, and Kent-Andre Mardal. *Automated solution of differential equations by the finite element method. The FEniCS book*. Springer, 2012.

[23] Martin Alnæs, Anders Logg, Kristian Oelgaard, Marie Rognes, and Garth Wells. Unified form language: A domain-specific language for weak formulations of partial differential equations. *ACM Transactions on Mathematical Software*, 40(2):9:1–9:37, 03 2014.

[24] Robert C. Kirby and Anders Logg. A compiler for variational forms. *ACM Transactions on Mathematical Software*, 32(3):417–444, 09 2006.

[25] D. Kamensky and Y. Bazilevs. tIGAr: Automating isogeometric analysis with FEniCS. *Computer Methods in Applied Mechanics and Engineering*, 344:477 – 498, 2019.

[26] Holger Wendland. *Scattered Data Approximation*. Cambridge University Press, 2005.

[27] Davoud Mirzaei, Robert Schaback, and Mehdi Dehghan. On generalized moving least squares and diffuse derivatives. *IMA Journal of Numerical Analysis*, 32:983–1000, 2011.

[28] Ben Gross, Nathaniel Trask, Paul Kuberry, and Paul Atzberger. Meshfree methods on manifolds for hydrodynamic flows on curved surfaces: A generalized moving least-squares (GMLS) approach. *Journal of Computational Physics*, 409:109–340, 02 2020.

[29] Nathaniel Trask, Huaiqian You, Yue Yu, and Michael L. Parks. An asymptotically compatible meshfree quadrature rule for nonlocal problems with applications to peridynamics. *Computer Methods in Applied Mechanics and Engineering*, 343:151 – 165, 2019.

[30] Marco Pasetto. *Enhanced Meshfree Methods for Numerical Solution of Local and Nonlocal Theories of Solid Mechanics.* PhD thesis, 2019.

[31] F. Bobaru, J.T. Foster, P.H. Geubelle, and S.A. Silling. *Handbook of Peridynamic Modeling*. Modern Mechanics and Mathematics. Taylor & Francis, 2015.

[32] Florin Bobaru, Mijia Yang, Leonardo Frota Alves, Stewart A. Silling, Ebrahim Askari, and Jifeng Xu. Convergence, adaptive refinement, and scaling in 1D peridynamics. *International Journal for Numerical Methods in Engineering*, 77(6):852–877, 2009.

[33] Qiang Du, Max Gunzburger, R. Lehoucq, and Kun Zhou. A nonlocal vector calculus, nonlocal volume-constrained problems, and nonlocal balance laws. *Mathematical Models and Methods in Applied Sciences*, 23:493–540, 01 2013.

[34] Yu Leng, X. Tian, Nathaniel Trask, and J. Foster. Asymptotically compatible reproducing kernel collocation and meshfree integration for nonlocal diffusion. *SIAM J. Numer. Anal.*, 59:88–118, 2021.

[35] J. Kiendl, K.-U. Bletzinger, J. Linhard, and R. Wüchner. Isogeometric shell analysis with Kirchhoff-–Love elements. *Computer Methods in Applied Mechanics and Engineering*, 198(49):3902–3914, 2009.

[36] Josef Kiendl. *Isogeometric Analysis and Shape Optimal Design of Shell Structures.* PhD thesis, 03 2011.

[37] Josef Kiendl, Ming-Chen Hsu, Michael C.H. Wu, and Alessandro Reali. Isogeometric Kirchhoff-–Love shell formulations for general hyperelastic materials. *Computer Methods in Applied Mechanics and Engineering*, 291:280–303, 2015.

[38] D. Kamensky. Open-source immersogeometric analysis of fluid–structure interaction using FEniCS and tIGAr. *Computers and Mathematics with Applications*, 81:634–648, 2021. Development and Application of Open-source Software for Problems with Numerical PDEs.

[39] Si-Yong Xiong and G. Cao. Bending response of single layer MoS_2. *Nanotechnology*, 27 10:105701, 2016.

[40] Jin-Wu Jiang, Zenan Qi, Harold Park, and Timon Rabczuk. Elastic bending modulus of single-layer molybdenum disulfide MoS_2: Finite thickness effect. *Nanotechnology*, 24:435705, 10 2013.

[41] Hendrik Heinz, Tzu-Jen Lin, Ratan Kishore Mishra, and Fateme S. Emami. Thermodynamically consistent force fields for the assembly of inorganic, organic, and biological nanostructures: The interface force field. *Langmuir*, 29(6):1754–1765, 2013. PMID: 23276161.

[42] Thomas A. Halgren. The representation of van der Waals (vdW) interactions in molecular mechanics force fields: potential form, combination rules, and vdW parameters. *Journal of the American Chemical Society*, 114(20):7827–7843, 1992.